We are IntechOpen, the world's leading publisher of Open Access books Built by scientists, for scientists

7,400
Open access books available

194,000
International authors and editors

210M
Downloads

154
Countries delivered to

Our authors are among the
TOP 1%
most cited scientists

14%
Contributors from top 500 universities

WEB OF SCIENCE™
Selection of our books indexed in the Book Citation Index in Web of Science™ Core Collection (BKCI)

Interested in publishing with us?
Contact book.department@intechopen.com

Numbers displayed above are based on latest data collected.
For more information visit www.intechopen.com

Chapter

Orbital Angular Momentum Wave and Propagation

Pankaj Jha and Ke Wu

Abstract

Orbital angular momentum (OAM) techniques are exploited for a wide range of potential radiofrequency (RF) and electromagnetic applications, including megahertz-through-terahertz wireless systems, fiber-based and free-space optical communications and sensing, just like acoustic and any other wave-based counterparts. In those RF and electromagnetic applications, OAM wave is set to enable the development of high-speed and high-capacity communications, radar imaging, and sensing systems, among many others. In this chapter, a comprehensive comparison between plane wave and OAM wave propagation using a patch antenna as a radiator at 2.45 GHz is presented and discussed. This comparison allows the appreciation of the fundamental properties of the OAM wave when compared against its plane wave counterpart. For simplified comparison and discussion, we will use two abbreviated terms: PWPA for plane-wave patch antenna and OWPA for OAM wave patch antenna. PWPA refers to as planar patch antenna that produces plane waves in far-field, whereas patch antenna that delivers OAM waves in far-field is termed as OWPA. In this context, all physical quantities for wave propagation such as electric field, magnetic field, wave impedance, wave vector, velocity, pitch, and propagation constant are theoretically studied for OAM waves and compared with plane waves. First, OAM wave generation is studied through widely used uniform circular antenna array (UCAA) in literature. Then, plane wave patch antenna (PWPA) and OAM wave patch antenna (OWPA) are designed and verified through simulation and measurement. OWPA is designed with characteristic mode analysis (CMA) based on a lossy substrate to excite a twisting wave at a determined patch location. With this in mind, a comparative investigation of PWPA and OWPA is conducted for different physical parameters. Cylindrical near-field scan clearly shows a helical wave motion for OWPA, whereas a normal plane wave motion for PWPA. Furthermore, the comparison of plane wave and OAM wave propagation is demonstrated using the combination of a Tx–Rx antenna pair. It is observed that the overall signal from OWPA can be received with two PWPAs at an angle as OWPA has a dispersive beam. Moreover, the receiving antenna with a large aperture and plane wave horn antenna (PWHA) in the line of sight (LOS) range can also be used to receive the overall signal from OWPA. The received signal in PWPA–PWPA, OWPA–OWPA, OWPA–PWPA–PWPA, OWPA–PWHA Tx–Rx pairs is thoroughly compared and studied. Measured and simulated results for transmission are −30 dB for 0 dB input signal in OWPA–PWPA–PWPA and OWPA–PWHA cases, which are reasonably justified within the sensitivity/dynamic range of short-distance communication and radar sensing receivers.

Keywords: plane wave patch antenna (PWPA), OAM wave patch antenna (OWPA), plane wave propagation, OAM wave propagation, Gaussian and Bessel beam, OAM impedance, OAM pitch, vortex wave, propagation constant

1. Introduction

Electromagnetic (EM) waves have been known to human society since the sixteenth century when mariners observed that lightning strikes could deflect a compass needle. EM waves transport both energy and momentum, where the momentum is categorized into two types: linear momentum and angular momentum. Specifically, the angular momentum has one added component in connection with field polarization, namely spin angular momentum (SAM), and the other component associated with spatial field distribution, termed as orbital angular momentum (OAM). Allen et al. [1] first introduced the concept of OAM in the optical domain. The twisted radio waves are characterized by amplitude singularity along its beam axis, and helical phase front of $\exp(\pm jl\phi)$, where ϕ denotes azimuthal angle around the beam axis, $\pm$ indicates respectively clockwise and anticlockwise helical-phase front, and l corresponds to OAM index number, also called as topological charge, which suggests the number of twists in one wavelength [1]. OAM wave is widely investigated, and physical systems based on OAM wave have been implemented in the optical domain [2, 3]. Perhaps, the OAM research in microwave areas is focused on increasing the channel capacity of wireless communications by multiplexing different modes of OAM at a single frequency [4–6].

Current communications and satellite systems across the globe are based on linear and spin angular momentum (plane wave propagation). People have used all the dimensions of space, time, frequency, and polarization for multiplexing signals in the channel to achieve a maximum data rate. Foreseeing the nature of the emerging and connected world, scientists anticipate that we will need a data rate of terabit per second (Tbps) for transmission in a decade. Presently used means of wireless communication can support data rates only up to Gbps as we have utilized the maximum extent of resources to achieve this. So, there is the need for another degree of freedom to achieve the data rate of Tbps, which can be realized by multiplexing different OAM modes at a single frequency [7]. However, the practical adoption of OAM waves for long-distance wireless communication is unsuitable because of singularity (null) in the boresight direction of radiating fields [8, 9]. It has been shown through the aperture antenna theory that OAM capacity can be significantly increased for near-field applications by using an extended OAM receiving antenna [9]. In 2012, Tamburini et al. experimented through the transmission of a signal for 442 m using a helical reflector antenna to increase the channel capacity of a wireless communication link [10]. However, many controversies arose from whether OAM multiplexing is a subset of MIMO and OAM multiplexing cannot work in the far-field [11]. In 2018, NTT Japan demonstrated a 10 m OAM multiplexing experiment with uniform concentric circular array (UCCA) and OAM–MIMO multiplexing, achieving a milestone data rate of 100 Gbps [12]. Despite some controversies, the scientific community is searching for more mature research and development in OAM, OAM antenna, and its system-level implementation has gained momentum in the past decade.

Obviously, OAM has potential applications in optical fiber communication, free-space optical communication, radio communication, and acoustic communication [13]. Its applications mainly lie in high-speed and high-capacity communication,

radar, imaging, and particle manipulation in the optical domain. Initially, cylindrical lenses were used to generate Hermite–Gaussian (HG) beam for the OAM wave by combining different states of the HG beam [1], then spiral phase plates were deployed to generate OAM waves in the optical domain [14]. In the radio domain, a similar trend was followed, and most research activities initially were focused on the generation of OAM waves using spiral phase plates [14–17]. Then, spiral reflectors were used to generate vortex beams [10, 18]. Also, planar antenna topology was deployed to generate OAM waves using uniform circular antenna arrays (UCCA) [19–25]. In [26], a circular time-switched antenna array was studied to generate an OAM wave. The time switched method uses high-speed RF switches to sequentially activate each array element, thus allowing the concurrent generation of OAM modes at harmonic frequencies of the switching period. Furthermore, a traveling wave circular slot was implemented to generate OAM waves [27, 28]. In addition, slot- and SIW-based OAM antennas were also considered [29, 30]. As in the optical domain, metamaterials have been used to generate OAM waves, similar to that has been implemented in the radio domain categorized as reflective metamaterials [31–40] and transmissive metamaterials [41]. OAM has also found its place in the guided-wave structure [42–47]. OAM has found applications in the acoustic domain, and analogous to antenna array in radio, uniform circular transducer antenna arrays are immensely used to generate acoustic vortex beam [48–50]. In nature, the vortex wave can well be observed as a twisting wave around a black hole [51], the most recent study of twisting wave around M87 black hole in radio astronomy [52], and the helical wave around the hurricane having a center point with null energy similar to the case of OAM [53]. **Figure 1** summarizes the state-of-the-art antenna types studied and researched for generating and detecting OAM waves from GHz to THz.

However, these previous works are dedicated to developing OAM waves using uniform circular antenna array (UCAA), spiral phase plates, and OAM multiplexing using UCCA. Minimal efforts have been invested in research to generate an OAM beam using a single patch antenna [60–62], which is set to relieve from complex feed network and space utilization. In this work, single patch-based plane wave patch antenna (PWPA) and OAM wave patch antenna (OWPA) are deployed as a demonstrator model to compare key performance parameters of PWPA and OWPA. Moreover, the main objective of this work is to show a comprehensive comparison of plane wave and OAM wave and appreciate the fundamental and distinguished properties of the OAM wave against those of the plane counterpart. Analytical, simulation and measurement comparisons between them are carried out thoroughly. In addition, it shows how the OAM wave can be useful for certain wireless applications even though point-to-point wireless connectivity with OAM is still a challenge because of its divergence pattern. Nevertheless, it is promising for short-range radar sensing applications. In this chapter, a detailed theoretical formulation of vector potentials, electric and magnetic fields for TE and TM modes, intrinsic impedances, wave vectors, propagation constants, wavelength, and pitch is devised and studied as a generic case for OAM waves. It shows clearly that the key performance parameters of plane waves are a special case of OAM waves. Furthermore, a narrative discussion of PWPA, OAM wave generation with single element patch using CMA, propagation, and characteristics comparison of PWPA and OWPA is carried out through simulations and validated through measurements.

Section 2 discusses the theoretical investigation of OAM wave and plane wave and their comparison in the rest of the chapter. Then, the OAM wave generation technique using UCCA is discussed in Section 3. This is followed by discussing simulated and measured results for PWPA and OWPA in Section 4. Subsequently, PWPA and

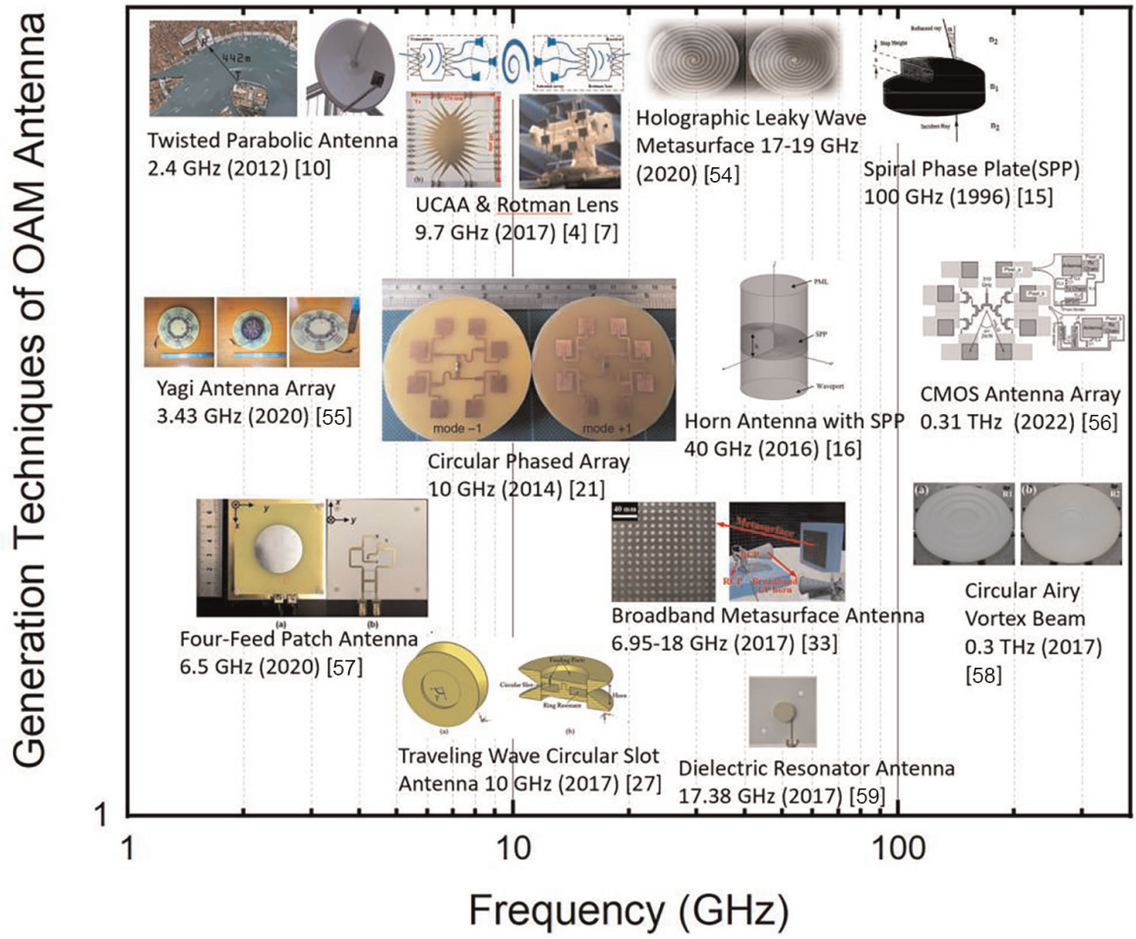

Figure 1.
State-of-the-art generation techniques of OAM wave using different antenna types from GHz to THz [54–59].

OWPA performances are compared critically in Section 5. Finally, plane wave propagation and OAM wave propagation are investigated and compared for different scenarios in Section 6. Then, concluding remarks are observed in Section 7.

2. Theoretical formulation of OAM and its comparison with plane wave

The set of nondiffractive Bessel beams solutions is based on the free-space differential Helmholtz equation, and their intensity profile has phase singularity with null amplitude at the center. The scalar form of Bessel beam skewing and propagating along the Z-axis in the cylindrical coordinates (ρ, ϕ, z) is given by [63]:

$$E\left(\vec{r}, t\right) = E_o J_l\left(k_\rho \rho\right) e^{j(k_z z - \omega t \pm l\phi)} \tag{1}$$

$$H\left(\vec{r}, t\right) = H_o J_l\left(k_\rho \rho\right) e^{j(k_z z - \omega t \pm l\phi)} \tag{2}$$

where E_o and H_o stand for amplitude; J_l is the lth order Bessel function of the first kind, k_ρ and k_z are the corresponding radial and longitudinal wave vectors satisfying the equation $k = 2\pi/\lambda = \sqrt{k_\rho^2 + k_z^2}$. The detailed derivation of the vector form of the Bessel beam is illustrated below.

2.1 Vector potential

The solution to wave equations in vector potential form is given by [64].

$$\nabla^2\vec{A} - \frac{1}{c^2}\frac{\partial^2\vec{A}}{\partial t^2} = 0 \tag{3}$$

Expanding it in the cylindrical coordinate (ρ, ϕ, z) yields

$$\begin{aligned}&\left[\frac{\partial^2 A_\rho}{\partial\rho^2} + \frac{1}{\rho}\frac{\partial A_\rho}{\partial\rho} + \frac{1}{\rho^2}\left(\frac{\partial^2 A_\rho}{\partial\phi^2} - A_\rho\right) + \frac{\partial^2 A_\rho}{\partial z^2} - \frac{2}{\rho^2}\frac{\partial A_\phi}{\partial\phi} - \frac{1}{c^2}\frac{\partial^2 A_\rho}{\partial t^2}\right]\hat{\rho}\\ &+\left[\frac{\partial^2 A_\phi}{\partial\rho^2} + \frac{1}{\rho}\frac{\partial A_\phi}{\partial\rho} + \frac{1}{\rho^2}\left(\frac{\partial^2 A_\phi}{\partial\phi^2} - A_\phi\right) + \frac{\partial^2 A_\varphi}{\partial z^2} + \frac{2}{\rho^2}\frac{\partial A_\rho}{\partial\phi} - \frac{1}{c^2}\frac{\partial^2 A_\phi}{\partial t^2}\right]\hat{\phi}\\ &+\left[\frac{\partial^2 A_z}{\partial\rho^2} + \frac{1}{\rho}\frac{\partial A_z}{\partial\rho} + \frac{1}{\rho^2}\frac{\partial^2 A_z}{\partial\phi^2} + \frac{\partial^2 A_z}{\partial z^2} - \frac{1}{c^2}\frac{\partial^2 A_z}{\partial t^2}\right]\hat{z}\\ &= 0\end{aligned} \tag{4}$$

where vector potential $\vec{A}$ is defined in the cylindrical coordinate system (ρ, ϕ, z) and (A_ρ, A_ϕ, A_z) are the scalar function. For the scenario when $A_\rho = A_\phi = 0$ and $A_z = \psi$, Eq. (4) reduces to

$$\frac{d^2\psi}{\partial\rho^2} + \frac{1}{\rho}\frac{d\psi}{d\rho} + \left(k_\psi^2 - k_z^2 - \frac{l^2}{\rho^2}\right)\psi = 0 \tag{5}$$

Hence, a set of Bessel beams is obtained by vector potential as

$$A_\rho = A_\varphi = 0; A_z\left(\vec{r}, t\right) = J_l\left(k_\rho\rho\right)e^{j(k_z z - \omega t \pm l\phi)} \tag{6}$$

where $k_z = k_\psi \cos(\alpha)$, $k_\rho = k_\psi \sin(\alpha)$, which can be deduced from **Figure 2**.

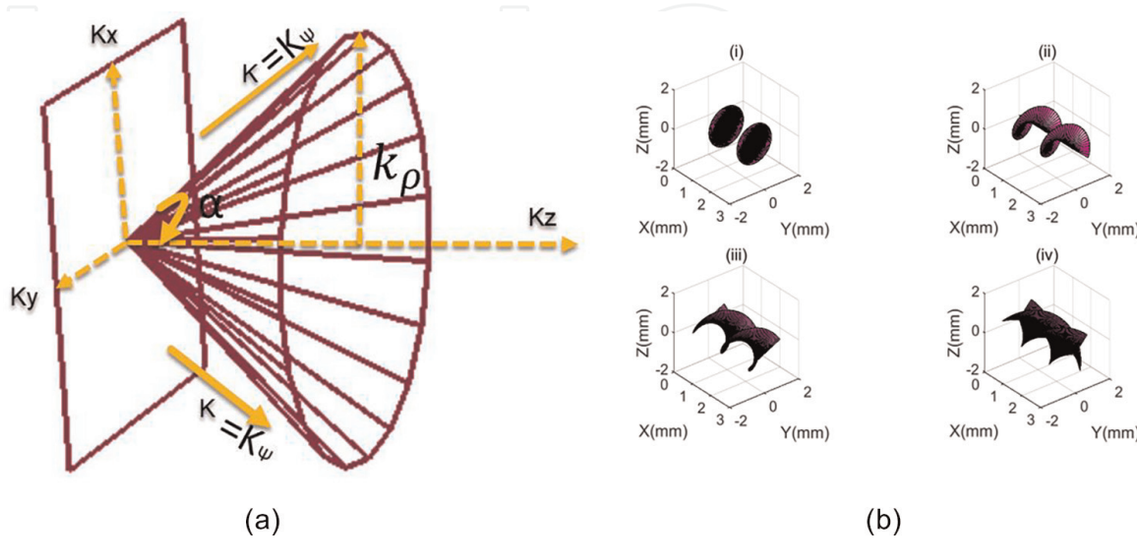

Figure 2.
(a) Plane-wave normal vectors making nondiffracting Bessel beam along the cone. A group of plane waves makes an angle α with the direction of propagation k_z to form an OAM wave. (b) 3-D phase front plot of OAM mode number (i) $l = 0$ (plane wave), (ii) $l = 1$, (iii) $l = 2$, (iv) $l = 3$.

2.2 Electric and magnetic field

The electric and magnetic fields can be obtained from vector potential $\vec{A}$ in the frequency domain form as

$$\vec{E} = -\nabla\Phi - \frac{1}{c}\frac{\partial A}{\partial t}; \vec{H} = \frac{1}{\mu}\nabla \times \vec{A} \tag{7}$$

After manipulating Eqs (6), (7), and using Lorentz condition, we obtain the electric and magnetic fields in a cylindrical coordinate system for TM and TE modes.

2.2.1 TM modes

$$\begin{bmatrix} E_\rho \\ E_\phi \\ E_z \end{bmatrix} = \begin{pmatrix} jk_\rho k_z \cos\alpha J_l'(k_\rho\rho) \\ \pm\frac{l}{\rho}k_z \cos\alpha J_l(k_\rho\rho) \\ k_\rho^2 \sin\alpha J_l(k_\rho\rho) \end{pmatrix} e^{j(k_z z - \omega t \pm l\phi)} \tag{8}$$

$$\begin{bmatrix} H_\rho \\ H_\phi \\ H_z \end{bmatrix} = \begin{pmatrix} \pm\frac{l}{\rho}\omega\varepsilon J_l(k_\rho\rho) \\ jk_\rho \omega\varepsilon J_l'(k_\rho\rho) \\ 0 \end{pmatrix} e^{j(k_z z - \omega t \pm l\phi)} \tag{9}$$

2.2.2 TE modes

Using the principle of duality ($E_{TE} = H_{TM};\ \ H_{TE} = -E_{TM}$)

$$\begin{bmatrix} E_\rho \\ E_\phi \\ E_z \end{bmatrix} = \begin{pmatrix} \pm\frac{l}{\rho}\omega\varepsilon J_l(k_\rho\rho) \\ jk_\rho \omega\varepsilon J_l'(k_\rho\rho) \\ 0 \end{pmatrix} e^{j(k_z z - \omega t \pm l\phi)} \tag{10}$$

$$\begin{bmatrix} H_\rho \\ H_\phi \\ H_z \end{bmatrix} = \begin{pmatrix} jk_\rho k_\rho \cos\alpha J_l'(k_\rho\rho) \\ \pm\frac{l}{\rho}k_z \cos\alpha J_l(k_\rho\rho) \\ k_\rho^2 \sin\alpha J_l(k_\rho\rho) \end{pmatrix} e^{j(k_z z - \omega t \pm l\phi)} \tag{11}$$

Clearly, all the electric and magnetic field components in TE and TM modes show azimuthal phase dependence with the OAM index number l and addition of extra elements to the exponential term. This is one of the possible solutions when $A_z = \psi$ and $A_\rho = A_\phi = 0$, and other possible solution can be considered as $A_\rho = \psi, A_\phi = \pm jA_\rho$ and $A_z = 0$. In this work, our focus is on the first case as it deals with linearly polarized OAM waves and the latter case corresponds to circularly polarized OAM waves, which is not the scope of this chapter as the antenna designed in further sections is also focused on a linearly polarized OWPA.

2.3 Key performance parameters for plane wave and OAM wave

In OAM, the wave travels helically around its longitudinal propagation direction, and this leads to define the pitch of OAM waves similar to the screw thread pitch

$$\text{Pitch of the OAM wave } (T_p) = \frac{2\pi l}{k_\psi \cos(\alpha)} = \frac{l\lambda_\psi}{\cos(\alpha)} \tag{12}$$

where $\lambda_\psi = \frac{2\pi}{k_\psi} = \frac{2\pi c}{\omega} = \lambda_{plane}$

As l = 0 the pitch of vortex waves vanishes, which can be seen from **Figure 2(b)**, indicating the formation of a plane wave phase front.

The wave vector is the position gradient of the phase of the Bessel beam

$$\vec{k} = \nabla(k_z z \pm l\phi) = k_z\hat{z} \pm \frac{l}{\rho}\hat{\phi} \tag{13}$$

where

$$k_{OAM}^2 = k_z^2 + \frac{l^2}{\rho^2} \rightarrow k = \sqrt{k_z^2 + \frac{l^2}{\rho^2}} \tag{14}$$

When Bessel beams with zero orbital angular momentum ($l = 0$; plane wave), the angular velocity is given by

$$\omega = k_\psi c = \frac{k_z c}{\cos\alpha} \tag{15}$$

So, the group velocity of OAM waves is obtained by the phase gradient of plane wave angular velocity, using Eq. (15)

$$\vec{V}_g = \nabla_k \omega = \frac{c}{\cos\alpha}\hat{z} \tag{16}$$

The intrinsic impedance of OAM waves in both TM and TE cases is obtained using Eq. (8) to (11)

$$\eta_{OAM_TM} = \frac{E_\rho}{H_\phi} = \frac{-E_\phi}{H_\rho} = \frac{k_z}{\omega\varepsilon}\cos\alpha = \eta_{plane}\cos\alpha \tag{17}$$

$$\eta_{OAM_TE} = \frac{\eta_{plane}}{\cos\alpha} \tag{18}$$

For plane-wave case $\alpha = 0$, which gives the classical value of the impedance of 377 Ω. This suggests that the generic form of the wave is actually an OAM wave, whereas the plane wave is a special case of OAM wave when $l = 0$ and $\alpha = 0$.

2.4 Propagation constant of plane wave and OAM wave in free space

The wavenumber in free space for OAM as in Eq. (14) and $k_z = k_\psi \cos\alpha$; This leads to

$$k_{OAM} = \sqrt{k_\psi^2 \cos^2(\alpha) + \frac{l^2}{\rho^2}} = \sqrt{\omega^2 \mu \varepsilon \cos^2(\alpha) + \frac{l^2}{\rho^2}} \tag{19}$$

In free space, the attenuation constant and phase constant of OAM waves are obtained as

$$\alpha_{OAM} = 0; \quad \beta_{OAM} = \sqrt{\omega^2 \mu_o \varepsilon_o \cos^2(\alpha) + \frac{l^2}{\rho^2}} \tag{20}$$

Special case: $\alpha = 0;\ \ l = 0$ (plane wave)

$$\alpha_{plane} = 0; \ \ \beta_{plane} = \omega\sqrt{\mu_o \varepsilon_o} = \frac{\omega}{c} \tag{21}$$

This gives us the attenuation and phase constant of the plane waves as a special case of the OAM waves.

We have derived all the physical quantities associated with wave propagation such as electric field, magnetic field, intrinsic impedance, wave vector, propagation constant, velocity, wavelength, and pitch of the OAM wave and compared it with the plane wave. By virtue of the derivation presented above, it brings us to the theoretical

Physical quantities	**Plane wave propagation**	**OAM wave propagation**
Electric field	$l = 0, k_p = 0, J_o(0) = 1$ $E\left(\vec{r}, t\right) = E_o e^{j(k_z z - \omega t)}$	$E\left(\vec{r}, t\right) = E_o J_l\left(k_\rho \rho\right) e^{j(k_z z - \omega t \pm l\phi)}$
Intrinsic impedance	$\eta_{plane} = \sqrt{\frac{\mu}{\varepsilon}}$ $\eta_{plane_FS} = \sqrt{\frac{\mu_o}{\varepsilon_o}} = 377$	$\eta_{OAM_TM} = \eta_{plane} \cos\alpha$ $\eta_{OAM_TE} = \dfrac{\eta_{plane}}{\cos\alpha}$
Wave vector and propagation constant	$k_\psi = k_z = \omega\sqrt{\mu\varepsilon} = \beta = \frac{2\pi}{\lambda}$ $k_\psi^2 = k_x^2 + k_y^2 + k_z^2 = \left(\frac{2\pi}{\lambda}\right)^2$ For free space, $k_\psi = \omega\sqrt{\mu_o \varepsilon_o} = \frac{\omega}{c}$ $\alpha_{plane} = 0$	$K_z = \sqrt{\omega^2 \mu\varepsilon - (l/\rho)^2} = K_\psi \cos(\alpha)$ $k_\rho = k_\psi \sin(\alpha)$ $k_{OAM}^2 = k_z^2 + k_\rho^2 = k_z^2 + \dfrac{l^2}{\rho^2}$ $k_{OAM} = \sqrt{\omega^2 \mu\varepsilon \cos^2(a) + \dfrac{l^2}{\rho^2}}$ For free space, $\alpha_{OAM} = 0$ $\beta_{OAM} = \sqrt{\omega^2 \mu\varepsilon \cos^2(\alpha) + \dfrac{l^2}{\rho^2}}$
Velocity	Phase velocity, $V_p = \frac{\omega}{k}\hat{k}$ Angular velocity, $\omega = \frac{k_z c}{\cos(\alpha)}\hat{z}$	Group velocity, $V_g = \frac{c}{\cos(\alpha)}\hat{z}$
Wavelength	$\lambda_z = \frac{2\pi}{k_z}$	$\lambda_z = \frac{2\pi}{k_z \cos(\alpha)} = \frac{\lambda_{FS}}{\cos(\alpha)}$
Wave vector	$\vec{k} = k_z \hat{z}$	$\vec{k} = k_z \hat{z} \pm \frac{l}{\rho}\hat{\phi}$
Pitch	0	$T_p = \frac{2\pi l}{k_\psi \cos(\alpha)} = \frac{l\lambda_\psi}{\cos(\alpha)}$

Table 1.
Comparison of plane wave and OAM wave propagation.

comparison of plane wave propagation (Gaussian beam propagation; zero-order Bessel beam) and OAM wave propagation (Bessel beam propagation; higher-order Bessel beam) in **Table 1**. After careful investigation and comparison, it is understandable that the plane wave is the special case of the OAM wave when $\alpha = 0,\ \ l = 0$. **Figure 2(a)** shows that the conical beam pattern formed by the Bessel beam propagating along the z-axis and group of plane waves at an angle combines to create an OAM wave. Moreover, once we have all the derivations of physical quantities for the OAM wave, respective physical quantities of the plane wave can be deduced by substituting $\alpha = 0,\ \ l = 0$ as presented in **Table 1**. The phase front plot of the OAM wave for different index numbers is shown in **Figure 2(b)**. This plot clearly indicates that the OAM wave of zero-order has no pitch, but as the order of OAM increases, the number of pitches increases same as the order of OAM per wavelength. The number of helixes formed for the OAM wave depends on the OAM order.

3. Generation of OAM vortex beam using uniform circular antenna array

First, we have analyzed a circular antenna array with eight elements for generating the OAM wave propagation at a frequency (f = 2.45 GHz), which has been widely used in literature, as shown in **Figure 3**. The number of elements in UCCA determines the largest mode (l) generated by the array. The mode number is governed as per theory $-N/2 < l < N/2$, where N is the number of elements in the array. Therefore, for the eight elements array, the mode number that can be produced is $-4 < l < 4$. For an N-element UCCA, each patch element is fed by the same amplitude but with an incremental phase shift, as shown in **Figure 4**. The generation of a particular mode in UCAA is achieved by an interelement phase shift as $2\pi l/N$, where l is the OAM winding number.

The simulated reflection coefficient is well below -15 dB at $f = 2.45$ GHz, as depicted in **Figure 5**. A simultaneous excitation of each element with constant amplitude and differential phase shift, as shown in **Figure 4**, is incorporated in simulation to obtain the reflection coefficient. The simulated 3D radiation pattern in both dBi and linear scale is shown in **Figure 6**. It can clearly be visualized the amplitude null in the boresight direction along the z-axis.

Figure 7(a) depicts the orthographic view of the power flow of an antenna, which shows annular intensity cross sections with null energy at the center, and maximum

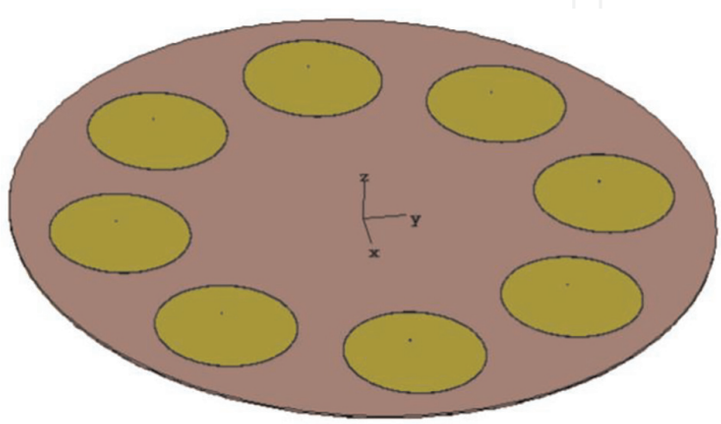

Figure 3.
Eight-element uniform circular antenna array (UCAA) for OAM antenna design.

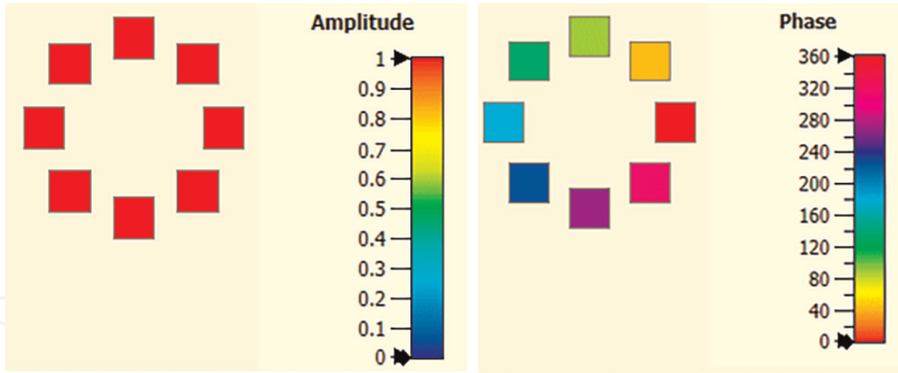

Figure 4.
Amplitude and phase excitation pattern of an eight-element array.

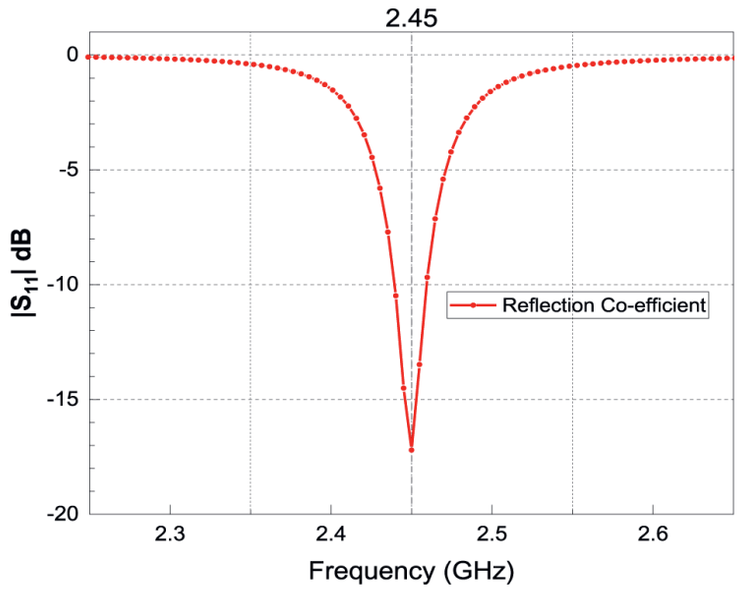

Figure 5.
Reflection coefficient of eight-element UCAA.

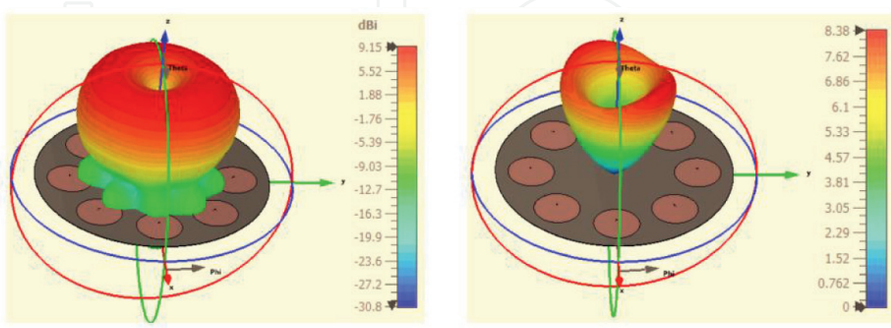

(a) (b)

Figure 6.
3D radiation pattern. (a) Realized gain (dBi) and (b) realized gain (linear).

energy is exhibited on the ring, satisfying the key characteristics of an OAM wave. This is shown for OAM mode $l = 1$, whereas for mode $l = 0$, beam power is at the center, forming the plane wave case. The twisted radio beams can be observed from the phase fronts of an OAM, as shown in **Figure 7(b)**.

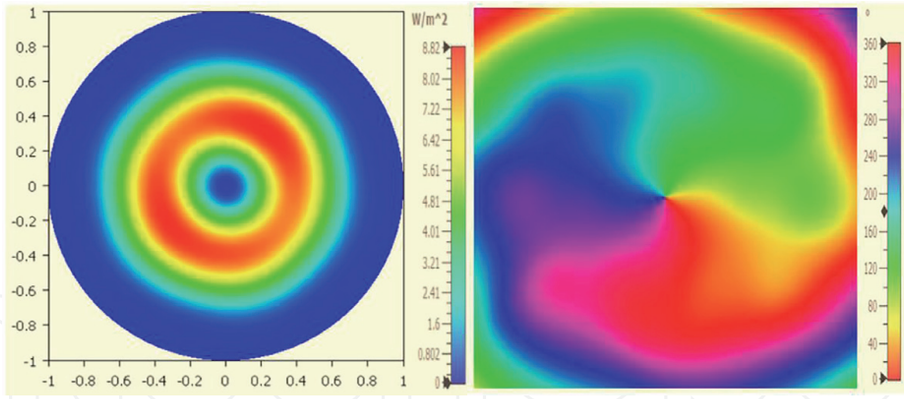

Figure 7.
(a) 2D plot of power flow of an antenna and (b) 2D plot of phase fronts of OAM mode 1 at cutplane $z = 32$ mm.

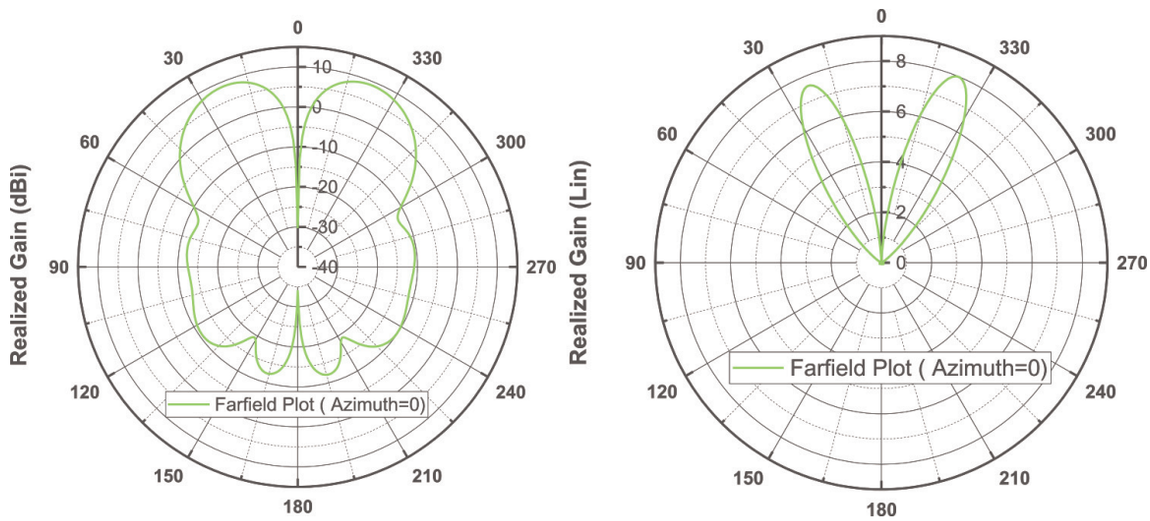

Figure 8.
1D polar plot of gain of a UCCA antenna. (a) Realized gain (dBi) and (b) realized gain (linear).

It is clearly observed in **Figure 8** that half-power null size from -33° to $+33^\circ$, and maximum gain of 9.15 dBi or 8 (linear scale) at 23°. The design of a uniform circular antenna array (UCCA) and uniform concentric circular antenna array (UCCAA) for generating particular OAM modes require a complex feed network. Its design becomes further complicated if multimodes OAM is generated simultaneously. Henceforth, in another section of this chapter, our discussion is on generating OAM waves using a patch antenna, which reduces the complexity of feed design.

4. PWPA and OWPA results and discussion

4.1 PWPA (plane wave patch antenna)

PWPA has been widely used in communications because it is one of the efficient radiators, with easy and low-cost fabrication and smooth integration with microwave circuits, and it supports linear and circular polarizations. In this work, the patch

antenna is designed at frequency $f = 2.45$ GHz for demonstration and comparison purposes on Rogers RT5880 substrate having dielectric constant ($\varepsilon_r = 2.2$), thickness ($t = 0.787\ mm = 30\ mils$), and loss tangent ($\delta = 0.0009$). The antenna has a coaxial probe feed from the ground plane, and it is located 6.4 mm in X-direction from the center point (0, 0, 0), as shown in **Figure 9**.

The designed procedure outline is based on the well-established cavity model formulation with a simulation model of circular microstrip patch antenna for the dominant mode TM^z_{lp0}. The radius (r) of the circular patch is determined for the desired resonant frequency at a given value of dielectric constant ε_r [65].

$$r = \frac{c}{2\pi\sqrt{\varepsilon_r}}\left(\frac{\chi'_{lp}}{f_{lp0}}\right) \tag{22}$$

where χ'_{lp} represents the zeros of the derivative of the Bessel function $J_l(x)$. A circular patch antenna has one degree of freedom, i.e., increasing the patch radius will decrease the resonant frequency and vice versa.

The CST Studio Suite® is utilized for the analysis of the patch antenna. 3D CAD is analyzed using a time-domain solver (FIT) and frequency-domain solver (FEM). The convergence of the S-parameter result is ensured from both the numerical techniques so that the simulated results match with measured results. The FIT solver technique on hexahedral mesh with Perfect Boundary Approximation® (PBA), to achieve a conformal meshing of the patch without having staircase approximation of mesh in 3D, is used for fast and accurate computation of fields in the patch, and the FEM solution is based on the tetrahedral mesh. The FIT solver is typically suited for electrically large and broadband problems as the requirement of hardware memory scale linearly with the number of mesh cells. In contrast, the FEM solver is suited for electrically small, narrowband, and resonant problems as the memory scale-up quadratically with the number of mesh cells [66].

The simulated and measured reflection coefficients of PWPA are plotted in **Figure 10**. PWPA is simulated with both FIT and FEM, which suggest a nearly perfect agreement with measurements. All the values are well below −30 dB, as depicted in **Figure 10**. The 1D polar plot and 3D radiation pattern plot of realized gain (dBi and linear) are depicted in **Figure 11**. All the plots show 7 dBi of realized gain in simulation, whereas 5 dBi in measurement, offset of merely 2 dB in measurement versus

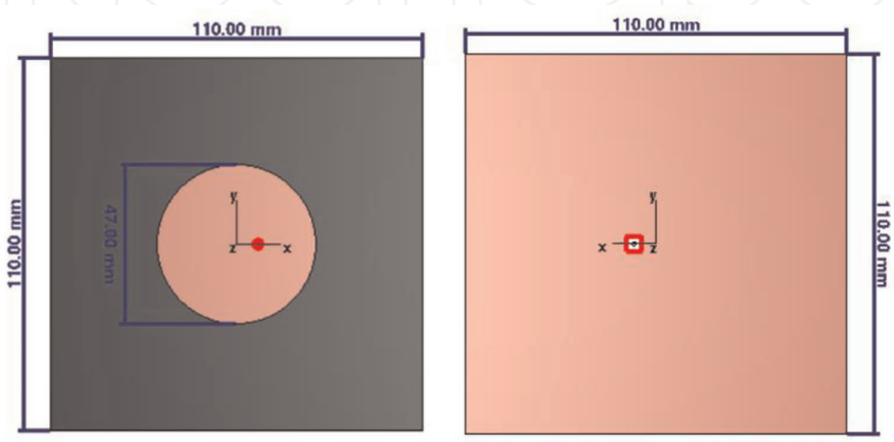

Figure 9.
Front and back view of simulated plane wave circular patch antenna in CST studio suite®.

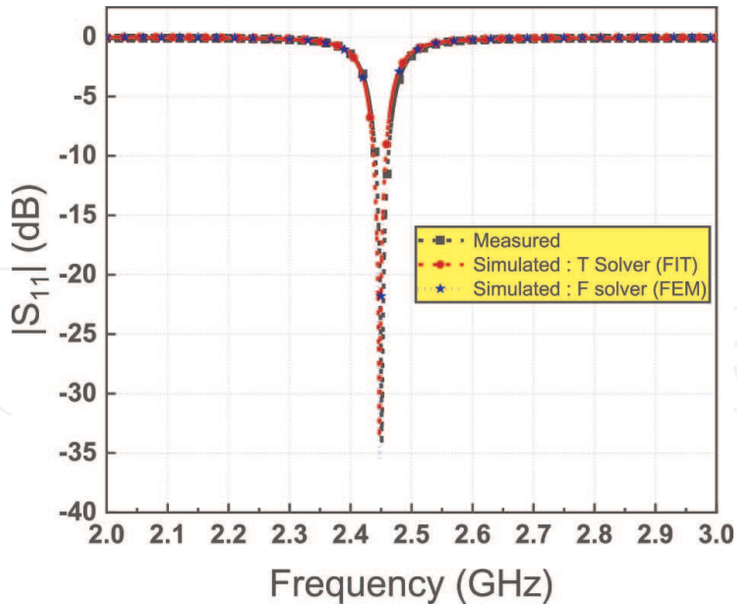

Figure 10.
Simulated and measured reflection coefficient of PWPA.

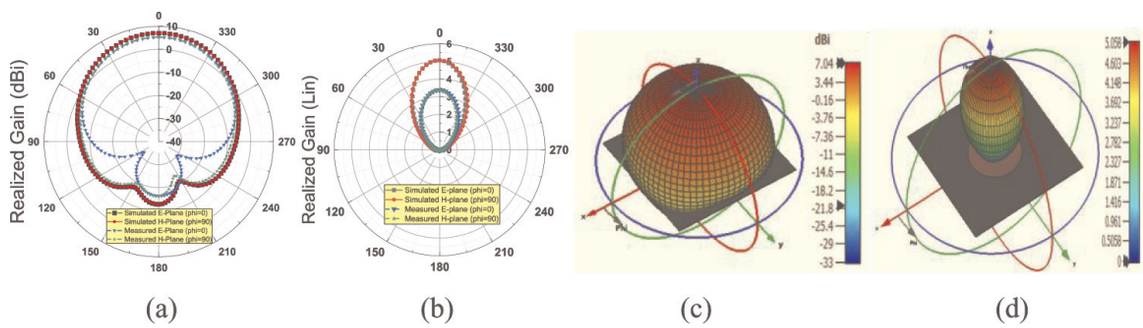

Figure 11.
(a) 1D polar plot of simulated and measured realized gain for E-plane and H-plane realized gain in dBi, and (b) realized gain in linear. (c) Plot of simulated 3D radiation pattern realized gain in dBi, and (d) realized gain in linear.

simulation. This offset is attributed to surface wave loss, dielectric loss, and exclusion of the connector model in simulation. On a linear scale, the realized gain in simulation is 5, while the measurement is 3.5.

4.2 OWPA (OAM wave patch antenna)

In literature, the OAM wave antenna has generally been designed with a UCCA and complex feed structure. In this work, we designed an unsymmetrical patch antenna [67, 68] by identifying a particular feed location where the patch will produce the OAM wave. The OWPA parameters are the same as those of PWPA. The red dot indicates the position of coaxial feed at X=8.75 mm, Y=21 mm from the center point of the antenna, as shown in **Figure 12**. Before a full-wave analysis of this antenna, characteristic mode analysis (CMA) is performed to examine the distribution of electric field and surface current on the antenna and excite the particular mode such that it is set to generate the desired OAM wave. The modal approach has been widely popular in the research community to design novel antennas for various applications, whereas CMA is gaining its popularity because it provides insight for improved

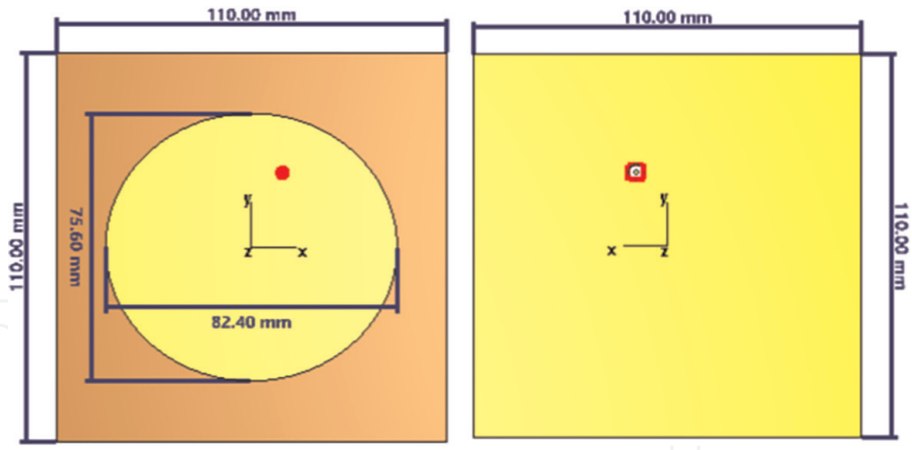

Figure 12.
Front and back view of simulated OWPA in CST studio suite®.

antenna design. CMA is a modal analysis (without excitation) for radiating structures or infinite open structures, whereas eigenmode analysis is for cavity structure or cavity filter design. The main advantage of CMA is to provide a better physical understanding of the surface current and field behavior of an antenna, which helps improve antenna design or postulate new antenna ideas. CMA provides valuable information such as resonant frequencies of inherent modes, far-field modal radiation patterns, modal surface currents on the analyzed structure, and modal significance at given frequencies. CMA can provide insight into the physical phenomena of an antenna of arbitrary shape and thus facilitate the analysis, synthesis, and optimization of antennas.

In the CMA theory, a generalized eigenvalue problem is solved. The generalized eigenvalue problem is given as follows [69]:

$$XJ_n = \lambda_n RJ_n \tag{23}$$

where R & X are real and imaginary Hermitian parts. J_n and λ_n are real eigenvectors and eigenmodes of the nth order mode. There are two main parameters that should be investigated while performing the CMA, which is given in the following:

Model significance (MS): MS is an intrinsic property that signifies the coupling capability of each characteristic mode with external sources. Individual mode contribution for the EM response of a given source is pointed by modal significance. It is easier to use MS rather than eigenvalue to examine the resonance of a structure. For perfectly radiating mode, MS = 1 for λ_n = 0.

$$MS = \left|\frac{1}{1 + j\lambda_n}\right| \tag{24}$$

Characteristic angle (α_n): It sets forth the comprehension of the mode behavior near resonance. Mathematically, $\alpha_n = 180^\circ - \arctan(\lambda_n)$.

- For $\alpha_n = 180^\circ \Rightarrow$ Resonant Mode.
- For $\alpha_n = 90^\circ - 180^\circ \Rightarrow$ Mode associated will be inductive.
- For $\alpha_n = 180^\circ - 270^\circ \Rightarrow$ Mode associated will be capacitive.

In general, for a resonant mode, the following three criteria should be satisfied as

$$\lambda_n = 0, MS = 1, \alpha_n = 180^{\circ}.$$

In this work, CMA is performed for five modes tracking in CST Studio Suite® between 2 and 3 GHz, and it is found that mode 1 (f = 2.3345 GHz) and mode 3

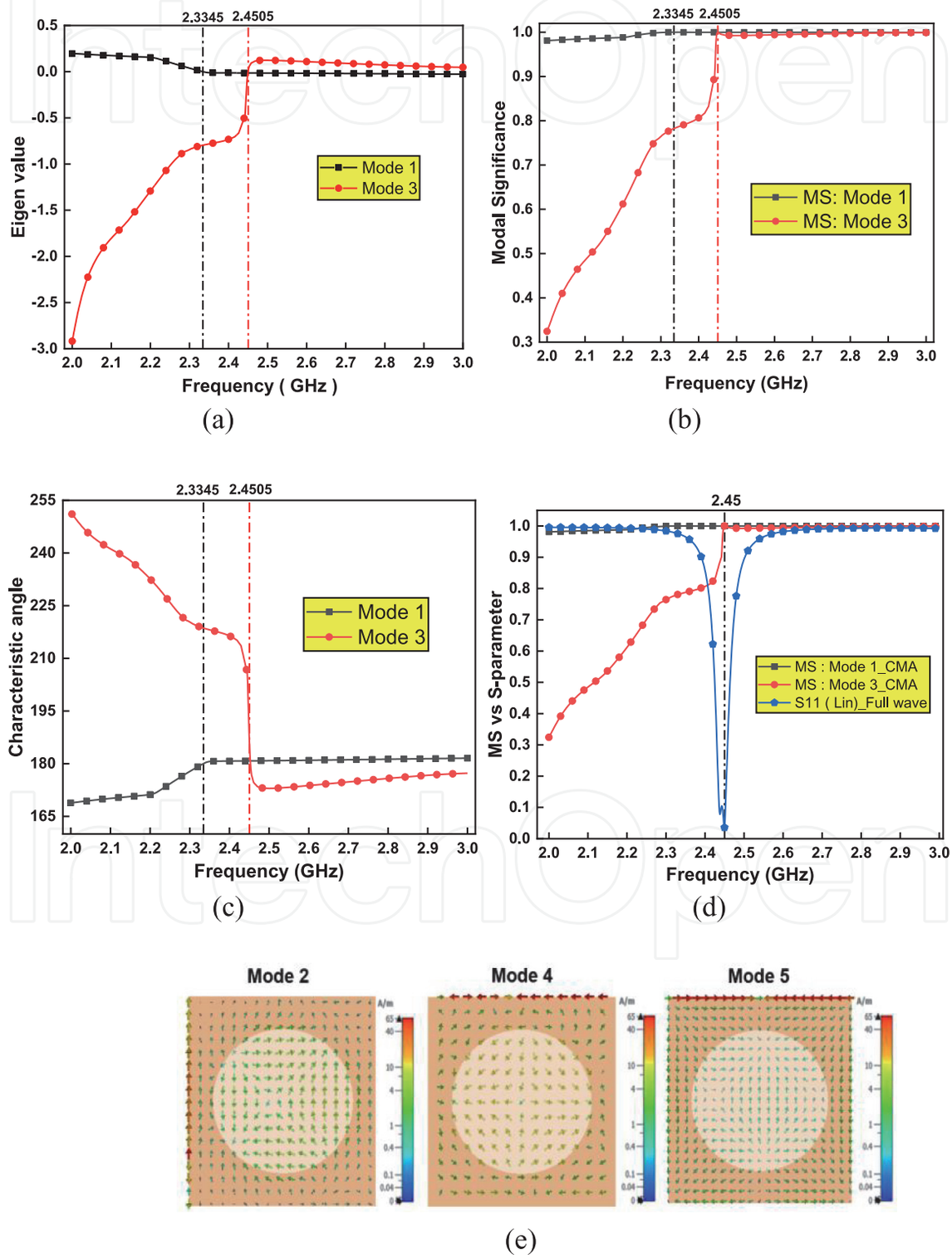

Figure 13.
Simulated (a) eigenvalue, (b) modal significance, (c) characteristic angle, and (d) MS vs. S-parameter using CMA in CST–MWS, (e) surface current of mode 2, mode 4, and mode 5.

(f = 2.4505 GHz) are the primary contributing modes for radiation. Mode 2, mode 4, and mode 5 have MS approaching 1 but do not satisfy all three resonant mode criteria. Moreover, the surface current of mode 2, mode 4, and mode 5 does not have null energy at the center, as shown in **Figure 13(e)**; the desired characteristic for twisting wave generation, henceforth, has been removed from further analysis. In addition, among mode 1 to mode 5, which are the most contributing modes, are determined by studying the nature of surface currents, electric fields, and far-field radiation behaviors of different CMA modes. Two orthogonal CMA modes are combined to form a full-wave analysis mode. The modal radiation quality factor is calculated as in Eq. (25). **Table 2** shows all five modes sorted at 2.45 GHz, resonance frequencies, Q-factors, and MS. Upon performing CMA, the plot of the significance of the modes sorted over frequency, in other words, which mode is contributing as the strongest to the radiation from the antenna at a given frequency (f = 2.45 GHz) is obtained in **Figure 13(b)** [70].

$$Q_n = \frac{\omega}{2}\left|\frac{d\lambda_n}{d\omega}\right|\Bigg|_{\omega=\omega_{res}} \tag{25}$$

We can also directly obtain the surface current distribution, electric and magnetic field, and far-field plot for all the modes at a given frequency of interest at 2.45 GHz using CMA.

In addition, overlaying the full-wave S-parameter curve on the modal significance plot as depicted in **Figure 13(d)** immediately shows which CMA mode is contributing to the resonances observed in the driven S parameter curve. In fact, for a given feed point, we can see a strong correlation between the driven mode currents and the CM currents. It is worth noting that when we drive the antenna, there is a contribution from all the modes at this frequency. Therefore, we cannot expect a perfect correlation. CMA is performed with metallic and dielectric together, giving better information than the classical approach of calculating CMA without lossy dielectric substrate. **Figure 14** clearly signifies the full-wave mode at f = 2.45 GHz is a combination of two CMA modes, mode 1 (f = 2.3345 GHz) and mode 3 (f = 2.4505 GHz). Overall, this gives rise to zero surface current, electric field, and far-field radiation at the central axis of the antenna. Besides, it generates a spiral motion of the electric field, which is the desired characteristic for twisting waves. With this understanding through CMA, we determine the location of the feed of an antenna, which will contribute to mode 1 and mode 3. We choose the feed as a common location for the surface current of both mode 1 and mode 3 of an elliptical patch antenna.

In this way, we will tame a simple plane wave patch antenna to an OAM wave patch antenna. Simulated and measured reflection coefficients of OWPA are shown in **Figure 15**. OWPA are simulated with FIT and FEM, showing a nearly perfect agreement with measurements. All the reflection coefficient values are well below −30 dB,

Mode	Resonance frequency	Q-factor	MS
1	2.3345	1.20	0.999628
2	2.3505	1.28	0.999370
3	2.4505	33.52	0.998896
4	2.7915	1.00	0.995350
5	2.8519	0.98	0.994957

Table 2.
Parameters of CMA in CST studio suite®.

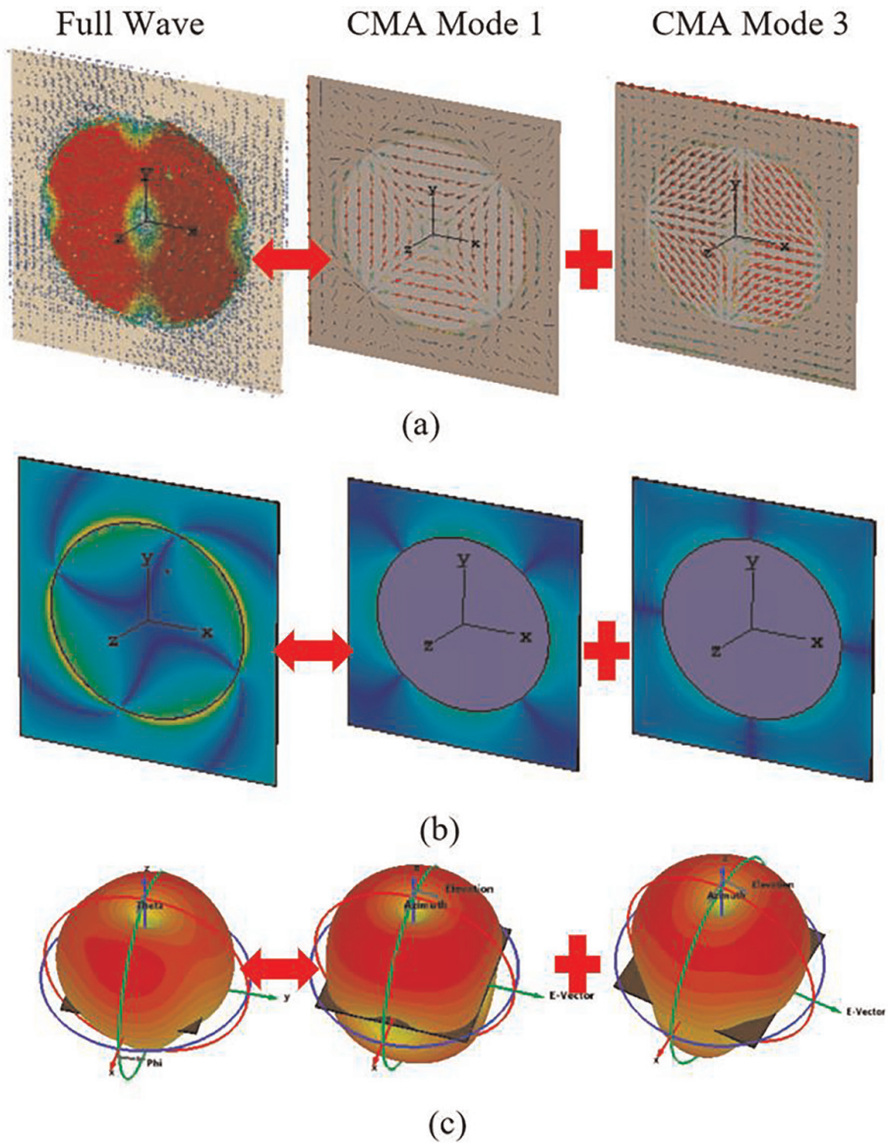

Figure 14.
Simulated (a) surface current, (b) electric field, (c) 3D radiation pattern for full-wave analysis, CMA mode 1 and mode 3 analysis.

as shown in **Figure 15**. The 1D polar plot of realized gain (dBi and linear) is depicted in **Figure 16**. The plots show 3.8 dBi of realized gain in simulation, whereas 1.8 dBi in measurement offset of merely 2 dB in simulation and measurement. On a linear scale, the realized gain in simulation is 2.5, whereas in measurement is 1.5.

5. Comparison of PWPA and OWPA

Until this point, the behavior of PWPA and OWPA is well understood, and it will be worth comparing the performance of these antennas. Let us begin with comparing the near-field electric field as depicted in **Figure 17(a)**, which shows a spiral motion of the electric field with null energy at the center for OWPA. At the same time, PWPA has energy at the central axis through an isoline pattern. **Figure 17(b)** also predicts similar behavior for PWPA and OWPA while showing their near-field magnetic field. It is worthwhile to visualize the E-near-field scan in **Figure 17(c)** on a cylindrical surface, which clearly indicates a helical motion of the electric field along the Z-axis

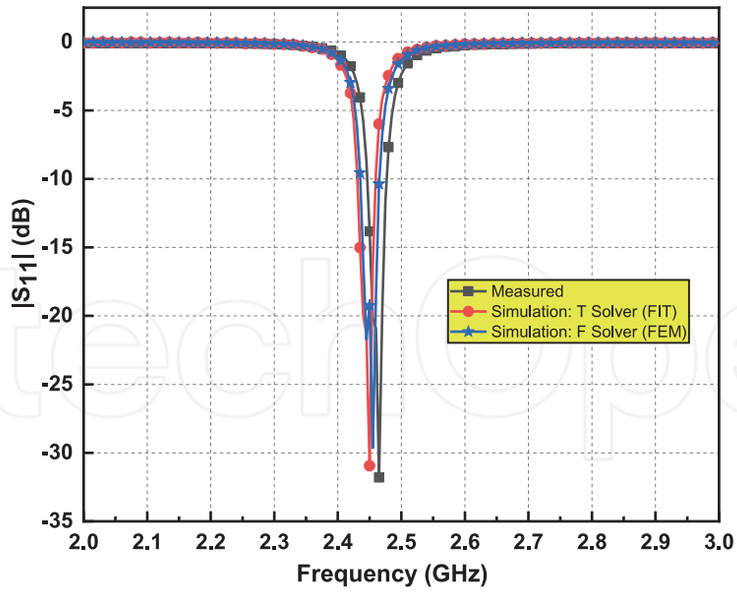

Figure 15.
Simulated and measured reflection coefficients of OWPA.

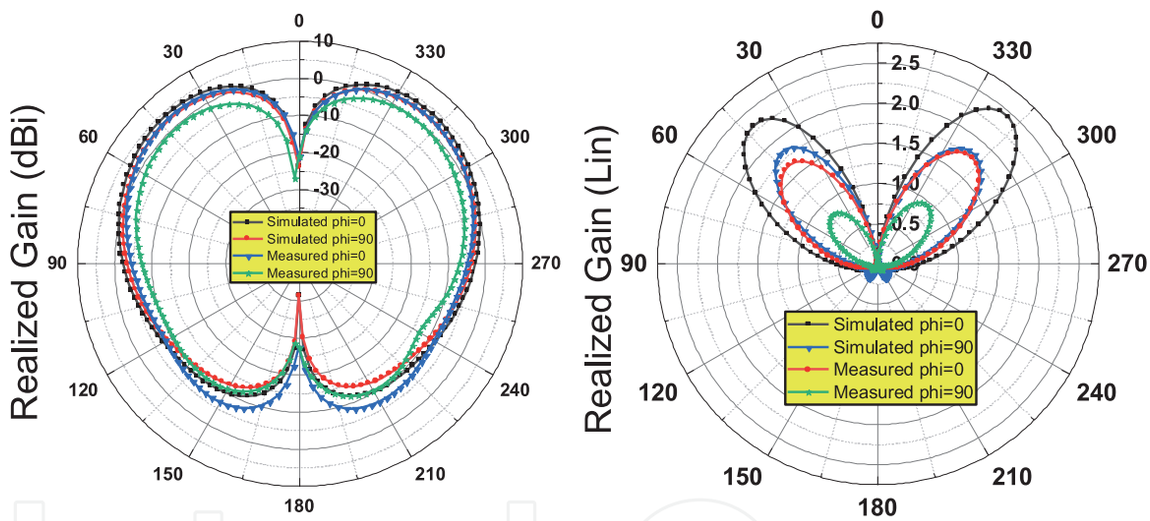

Figure 16.
1D polar plot of simulated and measured realized gain for E-plane and H-plane: (a) realized gain in dBi and (b) realized gain in linear.

(propagation axis) while the wave is advancing forward from OWPA. In contrast, the cylindrical scan for PWPA shows a typical plane wave pattern progressing normally in the direction of propagation. If we visualize the scenario in the cylindrical coordinate system (ρ, ϕ, z), E-field is swirling along the $\vec{\rho}$ and $\vec{\phi}$ orientation while advancing along the z-direction, precisely verified from Eq. (9) in theory.

This phase profile of the OAM beam is orthogonal to the propagation axis. The cylindrical scan is created for $h = 1$ m, $r = 5$ cm, and step size 1° in CST Studio Suite®. This shows us that PWPA has a uniform phase front, whereas the phase front of OWPA is changing with respect to $\exp(\pm jl\phi)$. This phase change pattern is also noted in **Figure 17(e)**, which shows twice the change 2π over a wavelength for OWPA, suggesting that OAM winding number or mode (l) 2 be produced. Comparing PWPA and OWPA through **Figure 17(d), (f)** and **(g)**, E-pattern in far-field (head-on), power flow (head-on), and 3D radiation pattern, respectively, simulated in CST-MWS, all

shows that Gaussian amplitude pattern of PWPA, whereas ring-like amplitude pattern for OWPA. Measured and simulated radiation patterns for E-plane and H-plane are demonstrated in **Figure 17(h)**, intriguingly showing a Gaussian pattern for PWPA, on the other hand, second-order Bessel beam pattern for OWPA. The radiation pattern is measured in our SATIMO starlab setup, as shown in **Figure 22**. It can be seen that merely 2 (lin) difference of the simulated and measured realized gain caused by the surface waves loss, dielectric loss in patch antenna, and 0.5 dB error in measurement in the SATIMO setup. The realized gain of PWPA is twice as much as OWPA, as the beam in OWPA is ring-like, and the gain is divided. Although PWPA has higher gain and power flow, OWPA power flow covered area is larger.

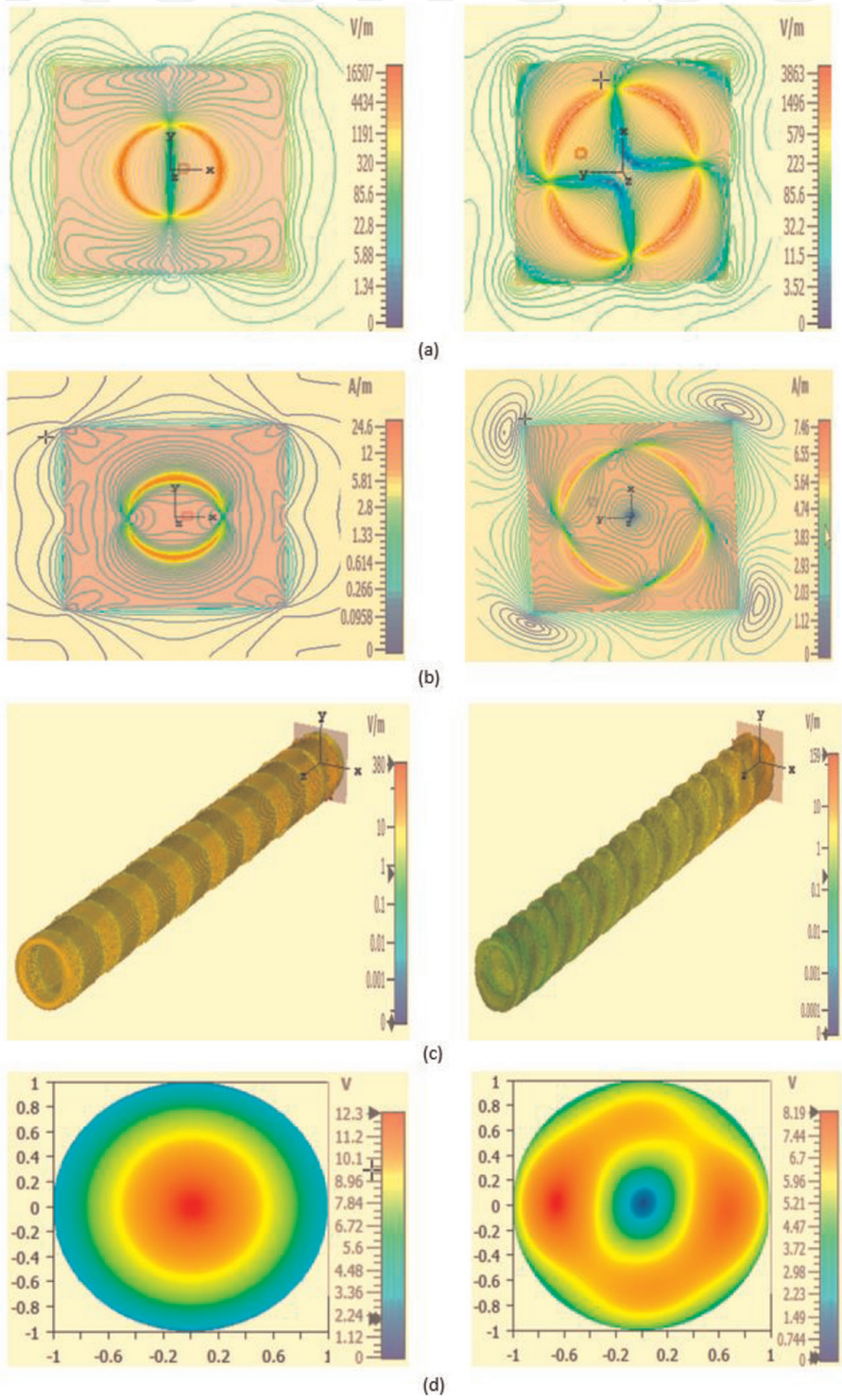

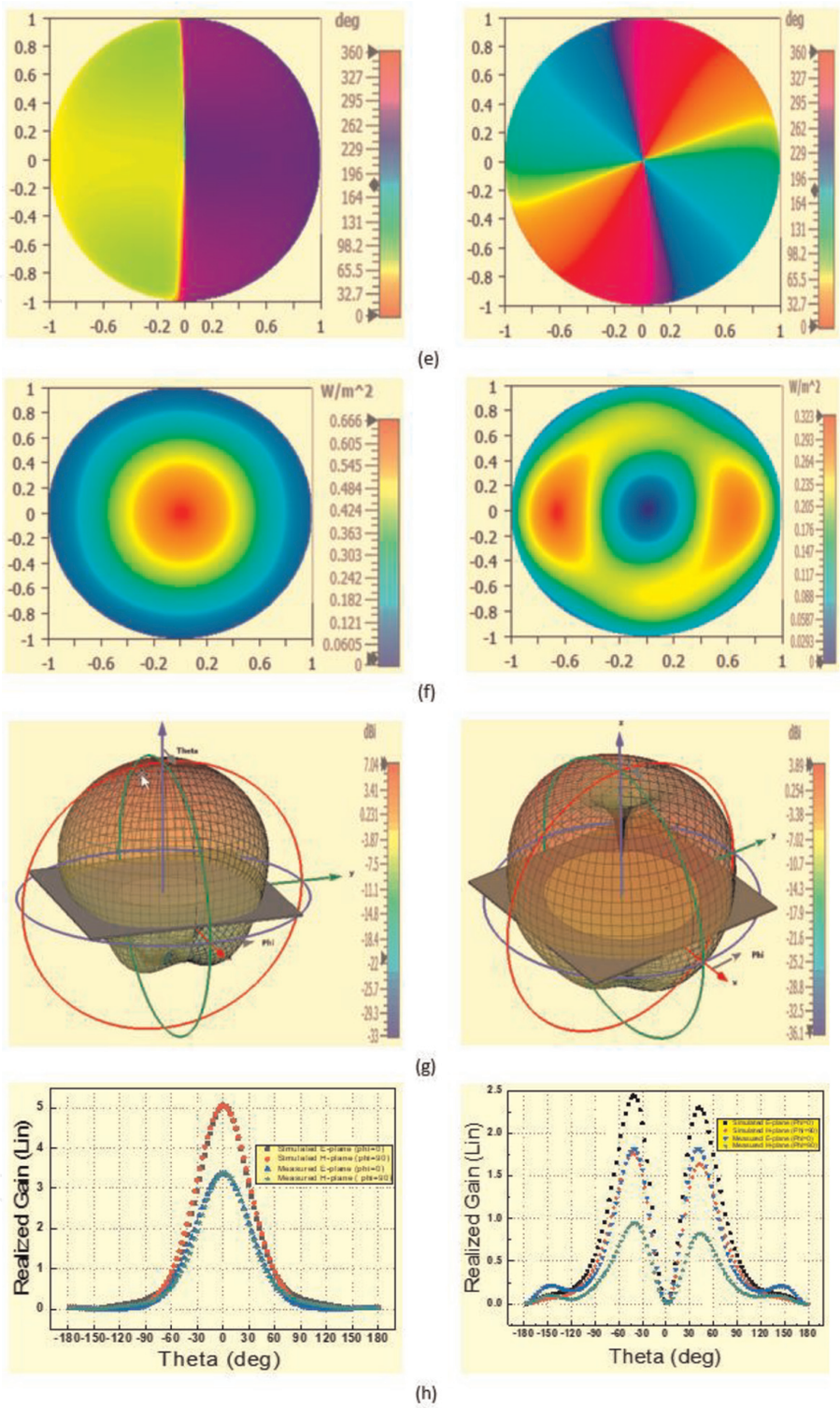

Figure 17.
Simulated PWPA (left) and OWPA (right). (a) E-field, (b) H-field, (c) cylindrical E-near-field scan, (d) E-pattern far-field, (e) phase pattern far-field, (f) power flow far-field, (g) 3D realized gain. Also, the 1D-polar plot of measured and simulated (h) realized gain (Lin) of PWPA and OWPA.

6. Comparison of plane wave and OAM wave propagation

This section compares plane wave and OAM wave propagation using PWPA and OWPA designed at frequency 2.45 GHz. The electrical size of PWPA or OWPA at the center frequency is 0.9λ. The PWPA or OWPA is enclosed in radiating bounding box

of size 1 m × 1 m × 1 m $\left(8\lambda \times 8\lambda \times 8\lambda; 512\lambda^3\right)$, as shown in **Figure 18(a)**. The extra open and added space radiating boundary ensures the far-field behavior in free space for both Tx–Rx antennas. The nature of the electric field, magnetic field, and power flow of individual PWPA, OWPA, and combined Tx–Rx pairs is monitored. Three cases simulated in the work are: (i) Tx–Rx: PWPA–PWPA, (ii) Tx–Rx: OWPA–OWPA, (iii) Tx–Rx–Rx: OWPA–PWPA–PWPA. In **Figure 18(a)**, two PWPA antennas, such as Tx and Rx, are separated by 1 m in their far-field distance.

Similarly, in the second case, **Figure 18(a)**, OWPA–OWPA Tx–Rx pair analysis is performed within the same boundary box as another simulation setup. **Figure 18(b)** illustrates the third case of OWPA–PWPA–PWPA configuration. The electric field carpet plots for individual PWPA and OWPA are depicted in **Figure 18(c)** and **(d)**, respectively. It clearly shows no field components along the z-axis for OWPA, whereas a maximum of the electric field for PWPA takes place along the z-axis. In fact, the OWPA electric field is skewed and is at an angle of 41° at x–z, y–z, and y–x plane. It also suggests that the Poynting vector for OWPA is not along the z-axis, but it is skewed along the z-axis.

It is evident that OWPA does not have a beam in direct LOS, so in **Figure 18(b)**, two PWPA at an angle of 41° are placed as a receiver antenna to pick up the signal from OWPA. This ensures a maximum reception of the signal from the OWPA antenna. The angle of 41° alignment is chosen as the main lobe direction of OWPA is at ±41°. In this presentation, O1 is the OAM wave patch antenna, and P2 and P3 are the plane wave patch antennas. Moreover, the RF propagation path modeling for OWPA(O1)–PWPA(P2)–PWPA(P3) clearly shows the direction of power flow and the establishment of a communication path, as shown in **Figure 19(c)**. The OWPA–OWPA configuration depicted in **Figure 19(b)** shows that maximum energy reception does not happen if we consider choosing both Tx and Rx antennas as OWPA in direct line of sight (LOS). In contrast, this is not the case for plane wave propagation, as portrayed in **Figure 19(a)**.

It allows us to monitor the simulated and measured transmission and reflection in both plane wave and OAM wave propagation scenarios. Firstly, PWPA–PWPA simulated and measured reflection coefficients are shown in **Figure 20(a)**. Reflection coefficients are well below −20 dB for both Tx–Rx pairs, while the transmission coefficient is just above −30 dB. In **Figure 20(b)**, the results are presented for OWPA (O1)–PWPA (P2)–PWPA (P3) configurations, which are one of the desired arrangements for the OAM receiving scenario. Both simulated and measured transmission

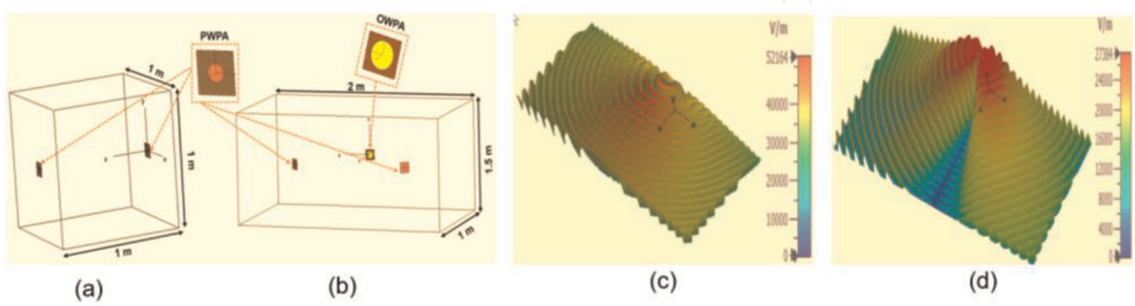

Figure 18.
(a) Far-field radiation condition in simulation to capture fields for PWPA–PWPA; (b) far-field radiation condition in simulation to capture fields for OWPA–PWPA–PWPA; (c) carpet plot of the electric field for PWPA and (d) OWPA on xz-plane gives visualization that PWPA has a maximum of propagation along the z-axis, whereas OWPA has no propagation along the z-axis. Propagation of OWPA is at an angle from the center of the z-axis.

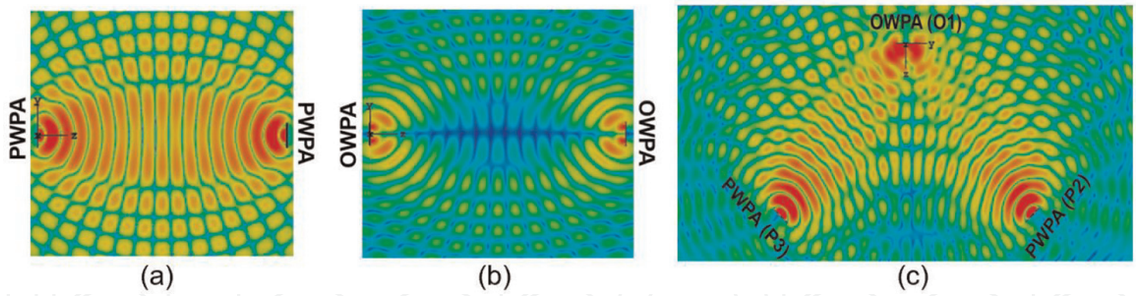

Figure 19.
RF propagation path modeling for (a) PWPA–PWPA, (b) OWPA–OWPA, (c) OWPA (O1)–PWPA (P2)–PWPA (P3). All the antennas are at the far-field distances, E-field is considered in depiction where red indicates maximum value, and blue represents minimum value.

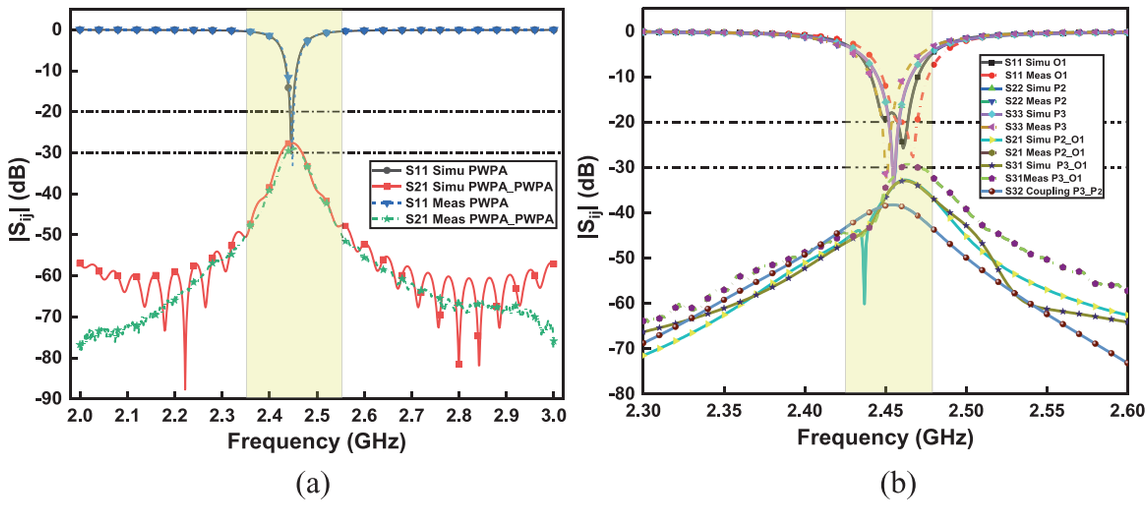

Figure 20.
Simulated and measured transmission and reflection coefficient of Tx–Rx pair (a) PWPA–PWPA and (b) OWPA (O1)–PWPA (P2)–PWPA (P3).

parameters for O1–P2 and O1–P3 are just above −30 dB, whereas all the reflection parameters are below −20 dB for all O1, P2, and P3. The frequency shift between the measured and simulated results is approximately 5 MHz, whereas the magnitude difference is negligible. All the measured results follow as designed and expected through simulation. The power received from two PWPA is combined, and the phase-detection method has to be used further in the system to know the order of OAM [70].

Furthermore, a comprehensive measured comparison of different configurations OWPA–OWPA, OWPA–PWPA, and OWPA–PWHA is shown in **Figure 21**. Among all these configurations, one of the least received signals is observed in OWPA–OWPA and the RF propagation path model, whereas the most robust signal is received in the case of OWPA–PWHA at −30 dB. OWPA–PWPA configuration has received a signal level just above OWPA–OWPA at −50 dB, as depicted in **Figure 21**.

It is worth noting that the acquired transmission behavior in **Figure 21** clearly shows the pattern of two peaks with a valley for all configurations, forming the M-shape as the desired characteristics for vortex reception, which cannot be observed in the O1–P2–P3 reception configuration in **Figure 20(b)**. The signal received at individual two PWPA should go through further a signal power combining technique to get the desired OAM pattern. The measurement setup for two configurations, PWPA–PWPA and OWPA–PWHA, is presented in **Figure 22**. The rest configuration is adopted similarly in measurement.

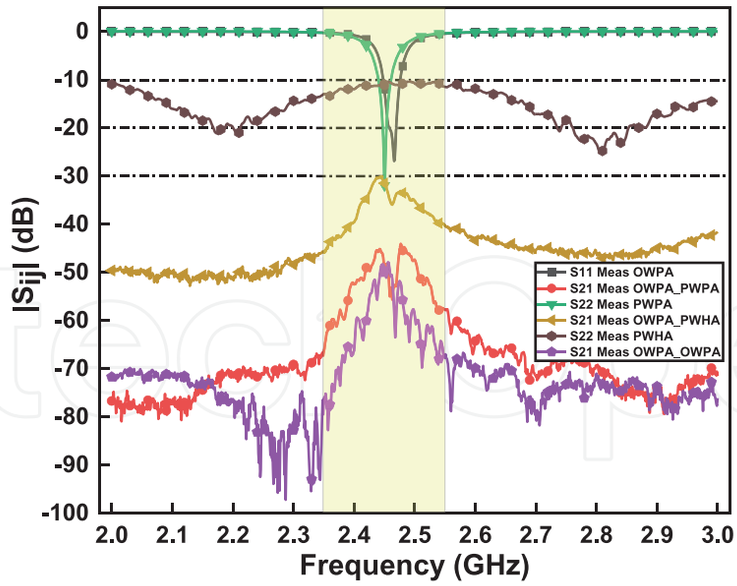

Figure 21.
Measured transmission and reflection coefficient of Tx–Rx pair OWPA–PWPA, OWPA–PWHA, OWPA–OWPA.

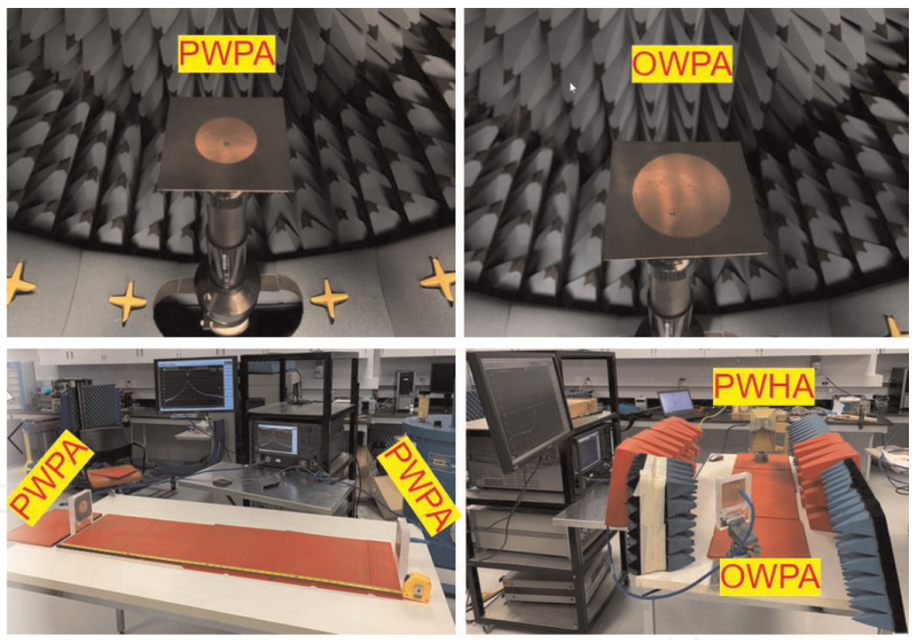

Figure 22.
Measurement setup in SATIMO lab and for Tx–Rx configuration.

7. Conclusions

This chapter provides a thorough analysis and comparison of the fundamental properties of plane wave and OAM wave in different Tx–Rx combinations using simulation, RF path modeling, and measurement to understand OAM reception techniques. The analytical equations for the electric field, magnetic field, and other physical parameters with respect to wave propagation have been derived and studied. Moreover, a comprehensive comparison of plane wave and OAM wave is examined in theory, designed PWPA and OWPA, and their propagation and reception

mechanisms. First of all, analytical equations of OAM wave have been developed and compared with those of plane wave. It is found that all the plane wave parameters can effectively be deduced from the modeling of OAM waves, which presents an excellent insight for understanding the differences between OAM wave and plane wave. Cylindrical near-field scan shows that the pitch of plane wave becomes zero while the OAM wave exhibits nonzero pitch through a helical motion along the direction of propagation. Subsequently, the designed PWPA and OWPA characteristics comparison is discussed in detail to show and appreciate the behavior of the patch antenna for the generation of plane wave and OAM wave. Moreover, a comparison of plane wave and OAM wave propagation is discussed and demonstrated that OWPA–PWHA and OWPA (O1)–PWPA (P2)–PWPA (P3) are favorable mechanisms for the reception of OAM signals.

Nevertheless, these comparisons provide a detailed understanding of propagation behavior, theory, and modeling for plane wave and OAM wave using a simple patch antenna concept. Furthermore, OAM wave can be used for short-range radar sensing and opportune the different paradigm in vortex wave.

Acknowledgements

The authors would like to thank Traian Antonescu, Maxime Thibault, Jules Gauthier, and Louis Philippe of the Poly-Grames Research Center, Polytechnique Montreal, Montreal, QC, Canada, for their support in fabrication and measurements.

Author details

Pankaj Jha and Ke Wu*
Department of Electrical Engineering, Poly-Grames Research Center, Polytechnique Montréal, Montréal, QC, Canada

*Address all correspondence to: ke.wu@ieee.org

IntechOpen

© 2022 The Author(s). Licensee IntechOpen. This chapter is distributed under the terms of the Creative Commons Attribution License (http://creativecommons.org/licenses/by/3.0), which permits unrestricted use, distribution, and reproduction in any medium, provided the original work is properly cited.

References

[1] Allen L, Beijersbergen MW, Spreeuw RJC, Woerdman JP. Orbital angular momentum of light and the transformation of Laguerre–Gaussian laser modes. Physical Review A. 1992; **45**(11):8185-8189. DOI: 10.1103/PhysRevA.45.8185

[2] Allen L, Barnett SM, Padgett MJ. Optical Angular Momentum. New York, NY, USA: CRC Press, Taylor & Francis Group; 2003

[3] Zettili N. Quantum Mechanics: Concepts and Applications. 2nd ed. Chichester, UK: Wiley; 2009

[4] Lee D, Sasaki H, Fukumoto H, Hiraga K, Nakagawa T. Orbital angular momentum (OAM) multiplexing: An enabler of a new era of wireless communications. IEICE Transactions on Communications. 2017;**E100.B**(7): 1044-1063. DOI: 10.1587/transcom.2016SCI0001

[5] Xu C et al. Free-space radio communication employing OAM multiplexing based on Rotman lens. IEEE Microwave and Wireless Components Letters. 2016;**26**(9): 738-740. DOI: 10.1109/LMWC.2016.2597262

[6] Oldoni M et al. Space-division demultiplexing in orbital-angular-momentum-based MIMO radio systems. IEEE Transactions on Antennas and Propagation. 2015;**63**(10): 4582-4587. DOI: 10.1109/TAP.2015.2456953

[7] Lee D, Sasaki H, Fukumoto H, Shiba H. Orbital angular momentum multiplexing technology towards the realization of Tbit/s wireless transmission. NTT Technical Review. 2017;**15**(9):9

[8] Zhao Y, Zhang C. Distributed antennas scheme for orbital angular momentum long-distance transmission. IEEE Antennas and Wireless Propagation Letters. 2020;**19**(2):332-336. DOI: 10.1109/LAWP.2019.2962199

[9] Morabito AF, Di Donato L, Isernia T. Orbital angular momentum antennas: Understanding actual possibilities through the aperture antennas theory. IEEE Antennas and Propagation Magazine. 2018;**60**(2):59-67. DOI: 10.1109/MAP.2018.2796445

[10] Tamburini F, Mari E, Sponselli A, Thidé B, Bianchini A, Romanato F. Encoding many channels on the same frequency through radio vorticity: First experimental test. New Journal of Physics. 2012;**14**(3):033001. DOI: 10.1088/1367-2630/14/3/033001

[11] Tamagnone M, Craeye C, Perruisseau-Carrier J. Comment on 'encoding many channels on the same frequency through radio vorticity: First experimental test'. New Journal of Physics. 2012;**14**(11):118001. DOI: 10.1088/1367-2630/14/11/118001

[12] Lee D et al. An experimental demonstration of 28 GHz band wireless OAM-MIMO (orbital angular momentum multi-input and multi-output) multiplexing. In: 2018 IEEE 87th Vehicular Technology Conference (VTC Spring), June. 2018. pp. 1-5. DOI: 10.1109/VTCSpring.2018.8417790

[13] Chen R, Zhou H, Moretti M, Wang X, Li J. Orbital angular momentum waves: Generation, detection and emerging applications. IEEE Communication Surveys and Tutorials. 2020;**22**(2):840-868. DOI: 10.1109/COMST.2019.2952453

[14] Beijersbergen MW, Coerwinkel RPC, Kristensen M, Woerdman JP. Helical-wavefront laser beams produced with a spiral phaseplate. Optics Communications. 1994;**112**: 321-327. DOI: 10.1016/0030-4018(94)90638-6

[15] Turnbull GA, Robertson DA, Smith GM, Allen L, Padgett MJ. The generation of free-space Laguerre–Gaussian modes at millimetre-wave frequencies by use of a spiral phase plate. Optics Communications. 1996;**127**: 183-188. DOI: 10.1016/0030-4018(96)00070-3

[16] Wei W, Mahdjoubi K, Brousseau C, Emile O. Horn antennas for generating radio waves bearing orbital angular momentum by using spiral phase plate. IET Microwaves, Antennas and Propagation. 2016;**10**(13):1420-1427. DOI: 10.1049/iet-map.2016.0064

[17] Shi CB, Li YB, Wu W, Wu RY, Cui TJ. An ultrathin spiral phase plate for generation of OAM radio waves. In: 2016 Progress in Electromagnetics Research Symposium, PIERS 2016; August 8, 2016-August 11, 2016; Shanghai, China. 2016. pp. 3740-3743. DOI: 10.1109/PIERS.2016.7735415

[18] Tamburini F, Mari E, Thidé B, Barbieri C, Romanato F. Experimental verification of photon angular momentum and vorticity with radio techniques. Applied Physics Letters. 2011;**99**:1-4. DOI: 10.1063/1.3659466

[19] Gong Y et al. Generation and transmission of OAM-carrying vortex beams using circular antenna array. IEEE Transactions on Antennas and Propagation. 2017;**65**(6):2940-2949. DOI: 10.1109/TAP.2017.2695526

[20] Spinello F, et al. Experimental near field OAM-based communication with circular patch array. July 2015. [Online]. arXiv:1507.06889 [physics]. Available from: http://arxiv.org/abs/1507.06889 [Accessed: 01 November 2020]

[21] Tennant A, Bai Q, Allen B. Experimental circular phased array for generating OAM radio beams. Electronics Letters. 2014;**50**(20): 1414-1415. DOI: 10.1049/el.2014.2860

[22] Deng C, Chen W, Zhang Z, Li Y, Feng Z. Generation of OAM radio waves using circular vivaldi antenna array. International Journal of Antennas and Propagation. 2013 Available from: h ttps://www.hindawi.com/journals/ijap/2013/847859/ [Accessed: 02 November 2020]

[23] Brousseau C, Mahdjoubi K, Emile O, Wei W. Generation of OAM waves with circular phase shifter and array of patch antennas. Electronics Letters. 2015; **51**(6):442-443. DOI: 10.1049/el.2014.4425

[24] Chen J. Performance evaluation of electromagnetic OAM waves with circular plate antenna array. In: 2019 International Conference on Communications, Information System and Computer Engineering (CISCE), July 2019, Haikou, China. 2019. pp. 226-229. DOI: 10.1109/CISCE.2019.00059

[25] Guo Z-G, Yang G-M. Radial uniform circular antenna array for dual-mode OAM communication. IEEE Antennas and Wireless Propagation Letters. 2017; **16**:404-407. DOI: 10.1109/LAWP.2016.2581204

[26] Tennant A, Allen B. Generation of OAM radio waves using circular time-switched array antenna. Electronics Letters. 2012;**48**(21):1365. DOI: 10.1049/el.2012.2664

[27] Zhang Z, Zheng S, Jin X, Chi H, Zhang X. Generation of plane spiral OAM waves using traveling-wave circular slot antenna. IEEE Antennas and Wireless Propagation Letters. 2017;**16**: 8-11. DOI: 10.1109/LAWP.2016.2552227

[28] Zhang W et al. Four-OAM-mode antenna with traveling-wave ring-slot structure. IEEE Antennas and Wireless Propagation Letters. 2017;**16**:194-197. DOI: 10.1109/LAWP.2016.2569540

[29] Gui L, Akram MR, Liu D, Zhou C, Zhang Z, Li Q. Circular slot antenna systems for OAM waves generation. IEEE Antennas and Wireless Propagation Letters. 2017;**16**:1443-1446. DOI: 10.1109/LAWP.2016.2641458

[30] Ke B, Li L, Wu Z, Bai J. Generation of dual-modes OAM beams based on SIW circular slot antenna. In: 2017 Sixth Asia-Pacific Conference on Antennas and Propagation (APCAP), October 2017, Xi'an. 2017. pp. 1-3. DOI: 10.1109/APCAP.2017.8420560

[31] Wu J, Zhang Z, Ren X, Huang Z, Wu X. A broadband electronically mode-reconfigurable orbital angular momentum metasurface antenna. IEEE Antennas and Wireless Propagation Letters. 2019;**18**(7):1482-1486. DOI: 10.1109/LAWP.2019.2920695

[32] Chen MLN, Jiang LJ, Sha WEI. Artificial perfect electric conductor-perfect magnetic conductor anisotropic metasurface for generating orbital angular momentum of microwave with nearly perfect conversion efficiency. Journal of Applied Physics. 2016;**119**(6): 064506. DOI: 10.1063/1.4941696

[33] Xu H, Liu H, Ling X, Sun Y, Yuan F. Broadband vortex beam generation using multimode Pancharatnam–berry metasurface. IEEE Transactions on Antennas and Propagation. 2017;**65**(12): 7378-7382. DOI: 10.1109/TAP.2017.2761548

[34] Yu S, Li L, Shi G, Zhu C, Zhou X, Shi Y. Design, fabrication, and measurement of reflective metasurface for orbital angular momentum vortex wave in radio frequency domain. Applied Physics Letters. 2016;**108**: 121903. DOI: 10.1063/1.4944789

[35] Yu S, Li L, Shi G. Dual-polarization and dual-mode orbital angular momentum radio vortex beam generated by using reflective metasurface. Applied Physics Express. 2016;**9**(8):082202. DOI: 10.7567/APEX.9.082202

[36] Yu S, Li L, Shi G, Zhu C, Shi Y. Generating multiple orbital angular momentum vortex beams using a metasurface in radio frequency domain. Applied Physics Letters. 2016;**108**(24): 241901. DOI: 10.1063/1.4953786

[37] Shi Y, Zhang Y. Generation of wideband tunable orbital angular momentum vortex waves using graphene metamaterial reflectarray. IEEE Access. 2018;**6**:5341-5347. DOI: 10.1109/ACCESS.2017.2740323

[38] Chen X, Zhou H, Liu M, Dong J. Measurement of orbital angular momentum by self-interference using a plasmonic metasurface. IEEE Photonics Journal. 2016;**8**(1):1-8. DOI: 10.1109/JPHOT.2015.2509859

[39] Zhang Y, Lyu Y, Wang H, Zhang X, Jin X. Transforming surface wave to propagating OAM vortex wave via flat dispersive metasurface in radio frequency. IEEE Antennas and Wireless Propagation Letters. 2018; **17**(1):172-175. DOI: 10.1109/LAWP.2017.2779269

[40] Yang L, Sun S, Sha WEI. Ultrawideband reflection-type

metasurface for generating integer and fractional orbital angular momentum. IEEE Transactions on Antennas and Propagation. 2020;**68**(3): 2166-2175. DOI: 10.1109/TAP.2019.2948711

[41] Qin F, Wan L, Li L, Zhang H, Wei G, Gao S. A transmission metasurface for generating OAM beams. IEEE Antennas and Wireless Propagation Letters. 2018; **17**(10):1793-1796. DOI: 10.1109/LAWP.2018.2867045

[42] Mao F, Li T, Shao Y, Huang M, Dong N. Generation of radio beams carrying OAM basing on coaxial waveguide. In: 2016 Progress in Electromagnetic Research Symposium (PIERS), August 2016, Shanghai, China. 2016. pp. 1267-1270. DOI: 10.1109/PIERS.2016.7734635

[43] Li Y, Xiao G, Li H. Generating radio OAM waves in circular waveguide with coaxial line feed structure. In: 2019 IEEE International Conference on Computational Electromagnetics (ICCEM), March 2019, Shanghai, China. 2019. pp. 1-3. DOI: 10.1109/COMPEM.2019.8779191

[44] Wei WL, Mahdjoubi K, Brousseau C, Sharaiha A, Emile O. Horn antenna for generating orbital angular momentum (OAM) waves. In: 2015 Loughborough Antennas & Propagation Conference (LAPC); November 2015; Loughborough, Leicestershire, United Kingdom. pp. 1-3. DOI: 10.1109/LAPC.2015.7365994

[45] Yang Y et al. Study of a water-immersed orbital angular momentum horn antenna. In: 2018 International Conference on Microwave and Millimeter Wave Technology (ICMMT); May 2018; Chengdu. 2018. pp. 1-3. DOI: 10.1109/ICMMT.2018.8563931

[46] Wei WL, Mahdjoubi K, Brousseau C, Emile O, Sharaiha A. Two monopole antennas for generating radio OAM waves in circular waveguide. In: 2016 10th European Conference on Antennas and Propagation (EuCAP); April 2016; Davos, Switzerland. 2016. pp. 1-4. DOI: 10.1109/EuCAP.2016.7481623

[47] Huang M, Zong X, Nie Z. Method to generate electromagnetic field with orbital angular momentum in circular waveguide. In: 2016 IEEE International Symposium on Antennas and Propagation (APSURSI); June 2016; Fajardo, PR, USA. 2016. pp. 1897-1898. DOI: 10.1109/APS.2016.7696655

[48] Deep-level stereoscopic multiple traps of acoustic vortices. Journal of Applied Physics;**121**(16) Available from: https://aip.scitation.org/doi/full/10.1063/1.4981122 [Accessed: 03 November 2020]

[49] Volke-Sepúlveda K, Santillán AO, Boullosa RR. Transfer of angular momentum to matter from acoustical vortices in free space. Physical Review Letters. 2008;**100**(2): 024302. DOI: 10.1103/PhysRevLett.100.024302

[50] Yang L, Ma Q, Tu J, Zhang D. Phase-coded approach for controllable generation of acoustical vortices. Journal of Applied Physics. 2013;**113**(15):154904. DOI: 10.1063/1.4801894

[51] Tamburini F, Thidé B, Molina-Terriza G, Anzolin G. Twisting of light around rotating black holes. Nature Physics. 2011;**7**(3) Art. no. 3. DOI: 10.1038/nphys1907

[52] Tamburini F, Thidé B, Valle MD. OAM radio astronomy—A new way to study the universe and its black holes. Royal Astronomical Society. 2020. p. 11

[53] Pan S, Wang L, Wang W, Zhao S. An effective way for simulating oceanic turbulence channel on the beam carrying orbital angular momentum. Scientific Reports. 2019;**9**(1) Art. no. 1. DOI: 10.1038/s41598-019-50465-w

[54] Oraizi H, Emamian H. Generation of orbital angular momentum modes via holographic leaky-wave metasurfaces. Scientific Reports. 2020;**10**(1):7358. DOI: 10.1038/s41598-020-64278-9

[55] Liu XY, Zhu Y, Xie W, Peng GH, Wang W. Generation of plane spiral orbital angular momentum waves by microstrip Yagi antenna array. IEEE Access. 2020;**8**:175688-175696. DOI: 10.1109/ACCESS.2020.3026241

[56] Khan MIW et al. A 0.31-THz orbital-angular-momentum (OAM) wave transceiver in CMOS with bits-to-OAM mode mapping. IEEE Journal of Solid-State Circuits. 2022:1-1. DOI: 10.1109/JSSC.2022.3141366

[57] Huang Y et al. Generation of broadband high-purity dual-mode OAM beams using a four-feed patch antenna: Theory and implementation. Scientific Reports. 2019;**9**(1):12977. DOI: 10.1038/s41598-019-49377-6

[58] Liu C, Liu J, Niu L, Wei X, Wang K, Yang Z. Terahertz circular airy vortex beams. Scientific Reports. 2017;**7**(1):Art. no. 1. DOI: 10.1038/s41598-017-04373-6

[59] Pan Y et al. Generation of orbital angular momentum radio waves based on dielectric resonator antenna. IEEE Antennas and Wireless Propagation Letters. 2017;**16**:385-388. DOI: 10.1109/LAWP.2016.2578958

[60] Barbuto M, Toscano A, Bilotti F. Single patch antenna generating electromagnetic field with orbital angular momentum. In: 2013 IEEE Antennas and Propagation Society International Symposium (APSURSI); July 2013. pp. 1866-1867. DOI: 10.1109/APS.2013.6711591

[61] Liu Y, Li W, Li Q, Zhu J. Rectangular patch antenna generating second-order vortex wave. In: 2019 Computing, Communications and IoT Applications (ComComAp), October 2019. 2019. pp. 358-360. DOI: 10.1109/ComComAp46287.2019.9018819

[62] Singh S, Upadhayay MD, Pal S. OAM wave generation using square-shaped patch antenna as slot array equivalence. IEEE Antennas and Wireless Propagation Letters. 2020;**19**(4):680-684. DOI: 10.1109/LAWP.2020.2976611

[63] McGloin D, Dholakia K. Bessel beams: Diffraction in a new light. Contemporary Physics. 2005; **46**(1):15-28. DOI: 10.1080/00107510420002752 59

[64] Hayt WH, Buck JA. Engineering Electromagnetics. 6th ed. Boston, MA, USA: Mc-Graw Hill; 2001

[65] Balanis CA. Antenna Theory Analysis and Design. 4th ed. Hoboken, New Jersey, USA: John Wiley & Sons, Inc.; 2016

[66] Studio CST. Training Manual. Darmstadt, Germany: Dassault Systemes Deutschland GmbH; 2021

[67] Shen L. The elliptical microstrip antenna with circular polarization. IEEE Transactions on Antennas and Propagation. 1981;**29**(1):90-94. DOI: 10.1109/TAP.1981.1142545

[68] Barbuto M, Trotta F, Bilotti F, Toscano A. Circular polarized patch antenna generating orbital angular momentum. PIER. 2014;**148**:23-30. DOI: 10.2528/PIER14050204

[69] Harrington R, Mautz J. Theory of characteristic modes for conducting bodies. IEEE Transactions on Antennas and Propagation. 1971;**19**(5):622-628. DOI: 10.1109/TAP.1971.1139999

[70] Mohammadi SM et al. Orbital angular momentum in radio: Measurement methods: OAM in radio-measurement methods. Radio Science. 2010;**45**(4):n/a-n/a. DOI: 10.1029/2009RS004299

IntechOpen